Investigating the properties of stripped-envelope supernovae; what are the implications for their progenitors?

S. J. Prentice [1,2★] C. Ashall,[2,3] P. A. James,[2] L. Short,[2] P. A. Mazzali,[2,4] D. Bersier,[2] P. A. Crowther,[5] C. Barbarino,[6] T.-W. Chen,[7] C. M. Copperwheat,[2] M. J. Darnley [2] L. Denneau,[8] N. Elias-Rosa,[9,10] M. Fraser [11] L. Galbany [12] A. Gal-Yam,[13] J. Harmanen,[14] D. A. Howell,[15,16] G. Hosseinzadeh,[15,16,24] C. Inserra [17] E. Kankare,[1] E. Karamehmetoglu,[6] G. P. Lamb [2,18] M. Limongi,[19,20] K. Maguire [1] C. McCully [15,16] F. Olivares E.,[21,22] A. S. Piascik,[2] G. Pignata,[21,23] D. E. Reichart,[25] A. Rest,[26,27] T. Reynolds [14] Ó. Rodríguez [21,23] J. L. O. Saario,[28,29,30] S. Schulze [13] S. J. Smartt,[1] K. W. Smith,[1] J. Sollerman,[6] B. Stalder,[31] M. Sullivan,[17] F. Taddia,[6] S. Valenti,[32] S. D. Vergani,[33] S. C. Williams [34] and D. R. Young[1]

Affiliations are listed at the end of the paper

ABSTRACT

We present observations and analysis of 18 stripped-envelope supernovae observed during 2013–2018. This sample consists of five H/He-rich SNe, six H-poor/He-rich SNe, three narrow lined SNe Ic, and four broad lined SNe Ic. The peak luminosity and characteristic time-scales of the bolometric light curves are calculated, and the light curves modelled to derive ^{56}Ni and ejecta masses (M_{Ni} and M_{ej}). Additionally, the temperature evolution and spectral line velocity curves of each SN are examined. Analysis of the [O I] line in the nebular phase of eight SNe suggests their progenitors had initial masses $<20\,M_{\odot}$. The bolometric light curve properties are examined in combination with those of other SE events from the literature. The resulting data set gives the M_{ej} distribution for 80 SE–SNe, the largest such sample in the literature to date, and shows that SNe Ib have the lowest median M_{ej}, followed by narrow-lined SNe Ic, H/He-rich SNe, broad-lined SNe Ic, and finally gamma-ray burst SNe. SNe Ic-6/7 show the largest spread of M_{ej} ranging from ~1.2–$11\,M_{\odot}$, considerably greater than any other subtype. For all SE–SNe $<M_{ej}> = 2.8 \pm 1.5\,M_{\odot}$ which further strengthens the evidence that SE–SNe arise from low-mass progenitors which are typically $<5\,M_{\odot}$ at the time of explosion, again suggesting $M_{ZAMS} <25\,M_{\odot}$. The low $<M_{ej}>$ and lack of clear bimodality in the distribution implies $<30\,M_{\odot}$ progenitors and that envelope stripping via binary interaction is the dominant evolutionary pathway of these SNe.

Key words: Supernovae: general.

1 INTRODUCTION

Stripped-envelope supernovae (SE–SNe, SNe Ib/c) are a subset of core-collapse events that arise from stars almost completely deficient in helium and/or hydrogen at the time of explosion. These events are named on the basis of their spectroscopic appearance. The presence of strong H α and other Balmer lines leads to an SN IIb event, those without clear H signatures but are strong in He are

SNe Ib, and those without traces of He are SNe Ic (see Filippenko et al. 1995; Matheson et al. 2001). Although there are potentially SNe Ic with traces of He in the ejecta (SN 2016coi; Yamanaka et al. 2017; Prentice et al. 2018a), the vast majority are incompatible with He (Modjaz et al. 2016; Taddia et al. 2018b).

In the classification scheme of Prentice & Mazzali (2017), the sequence of He-rich SNe was refined into four subclasses, each with progressively less evidence for H in the ejecta; SNe IIb, SNe IIb(I), SNe Ib(II), and SNe Ib. For SNe Ic, the classification was based upon quantifying the degree of line blending. Based upon a set of

common lines found in the optical spectra, the SNe were classified from narrow-lined to broad-lined as; SNe Ic-7, SNe Ic-6, SNe Ic-5, SNe Ic-4, and SNe Ic-3. SNe Ic-5 are the transition between broad lined (Ic-3/4) and narrow lined (Ic-6/7) events. This classification scheme is adopted through this work and can be approximated with the traditional taxonomy by assuming

(i) IIb + IIb(I) – H/He-rich SNe ∼ IIb
(ii) Ib + Ib(II) – H-poor/He-rich ∼ Ib
(iii) Ic-5/6/7 – narrow-lined SNe ∼ Ic
(iv) Ic-3/4 – non-GRB Ic-BL

The quantity of data on these SE types has rapidly increased in the last few years thanks to large data releases (e.g. Bianco et al. 2014; Taddia et al. 2015; Stritzinger et al. 2018a), which allows more in-depth study of their light curves (Drout et al. 2011; Lyman et al. 2016; ; Prentice et al. 2016; Taddia et al. 2018b) and spectroscopic properties (Liu et al. 2016; Modjaz et al. 2016; Prentice & Mazzali 2017; Fremling et al. 2018).

SE SNe typically rise on time-scales between 10 and 20 days, though some extreme events can be nearly 40 days (e.g. SN 2011bm, iPTF15dtg; Valenti et al. 2012; Taddia et al. 2016). The most extremely energetic events are defined by broad absorption lines in their spectra (Iwamoto et al. 1998), with some associated with X-ray flashes (XRF) and gamma-ray bursts (GRBs). GRB-SNe can have large ejecta masses, $M_{ej} \sim$ 8–12 $M_{\odot}$, and kinetic energy E_k that can exceed 10^{52} erg (see Nakamura et al. 2001; Mazzali et al. 2003, 2006; Olivares E et al. 2015). The extreme E_k of these events is thought to come from the rotational energy of a compact object (Woosley 1993; Mazzali et al. 2014; Ashall et al. 2017). There is also evidence that SE events are inherently aspherical (e.g. Mazzali et al. 2005; Maeda et al. 2008; Wang & Wheeler 2008; Tanaka et al. 2009; Chornock et al. 2011; Mauerhan et al. 2015; Stevance et al. 2016, 2017).

Progenitors of SE–SNe have been detected in pre-explosion imaging or colour-excess in post-explosion in photometry after the SN has faded, mostly for H-rich SE–SNe; SN 1993J (Aldering, Humphreys & Richmond 1994; Smartt 2009), SN 2008ax (Crockett et al. 2008; Arcavi et al. 2011; Folatelli et al. 2015), SN 2011dh (Maund et al. 2011), SN 2013df (Van Dyk et al. 2014), and SN 2016gkg (Kilpatrick et al. 2017; Tartaglia et al. 2017). In all cases, the progenitor star was estimated to have $M_{ZAMS} <$20 $M_{\odot}$. The progenitor of SN Ib iPTF13bvn was estimated to have $M_{ZAMS} =$10–20 $M_{\odot}$, and a possible binary companion (see Cao et al. 2013; Bersten et al. 2014; Fremling et al. 2014; Eldridge & Maund 2016).

There is currently only one progenitor candidate for SNe Ic, a $M_{ZAMS} =$47–80 $M_{\odot}$ star for Ic-7 SN 2017ein; however, the identification of the actual progenitor is uncertain and quite possibly the object identified is a compact star cluster (Van Dyk et al. 2018). The progenitors of SNe Ic are plausibly WO and WC Wolf–Rayet stars at the time of explosion (Crowther 2007). They are UV-bright but relatively dim in the optical and may be further attenuated by local dust formation (Crowther et al. 2003). This leads to difficulty in locating them in pre-explosion imaging (Smartt 2009; Eldridge et al. 2013).

In the absence of a progenitor candidate, another method is to estimate the age of the stellar population at the site of the explosion. Anderson et al. (2012) found that SNe Ib/c are more often associated with H α emission and interpreted this as evidence of stars from young populations and are therefore more massive than the typical progenitor for SNe II. Galbany et al. (2016) examined the host of nearby SNe and suggested that SNe Ib are the result of binary stripping but that some SNe Ic are likely single massive stars.

Similar results were found by Kuncarayakti et al. (2018), some SE–SNe favour low-mass progenitors but their stellar populations are typically younger. The stellar populations at the location of SNe Ic are often calculated to be the youngest, hence their progenitors are assumed to be the most massive (e.g. Galbany et al. 2018). Maund (2018) estimates that these SNe arise from stars >30 $M_{\odot}$. In the cases of specific SNe, Maund et al. (2016) estimates that the progenitor of SNe Ic-7 2007gr ($M_{ej} <$2 $M_{\odot}$; Mazzali et al. 2009) to be $M_{ZAMS} \sim$ 30 $M_{\odot}$. However, Crowther (2013) cautions against inferring stellar age from H II regions, as these can survive for tens of millions of years and give rise to several generations of massive stars and limits mass estimates in these regions to >12 $M_{\odot}$. Regardless, there is a propensity for SNe Ib and Ic to be found nearer to H II regions compared with SNe II.

For a single star, mass loss is an increasing function of initial mass, metallicity, and rotation. SE–SNe are ∼30 per cent of all core-collapse events in the local Universe and occur at relative volume-limited rate of $N_{IIb} \approx N_{Ib} \approx 0.8 N_{Ic}$ (Shivvers et al. 2017). These rates are not compatible with a purely mass-dominated regime. However, mass loss can also occur through envelope stripping via interaction with a close binary companion, allowing stars with lower initial masses than in the single star scenario to be stripped (e.g. Nomoto, Iwamoto & Suzuki 1995). The binary fraction of massive stars close enough to undergo mass transfer is 70 per cent in the Milky Way (Sana et al. 2012), so this is a physical process which affects most massive stars. There have been direct detections of binary companions to three stripped-supernovae; SNe 1993J, 2011dh, and 2001ig (Maund et al. 2004; Folatelli et al. 2014; Fox et al. 2014; Maund et al. 2015; Ryder et al. 2018). Upper limits have been placed on the mass of companions for Ic-6 SN 1994I (10 $M_{\odot}$; Van Dyk, de Mink & Zapartas 2016) and Ic-4 SN 2002ap (8–10 $M_{\odot}$, also used to limit the progenitor of SN 2002ap to $M_{ZAMS} <$23 $M_{\odot}$; Zapartas et al. 2017).

This work presents photometric and spectroscopic observations of 18 SE–SNe, observed between 2013 and 2018 as part of the Public ESO Spectroscopic Survey of Transient Objects (PESSTO), extended PESSTO (ePESSTO) (Smartt et al. 2015), and a Liverpool Telescope SE–SN follow-up campaign, and the Las Cumbres Observatory Supernova Key Project. The observations and data reduction methods are presented in Section 2. Section 3 presents the multicolour light curves, the bolometric light curve and modelling, and the temperature evolution of the SNe. In Section 4, the maximum light and nebular phase spectra are shown along with analysis of the line velocities. The results are set into context against other SE–SNe in Section 5, and in Section 6 ^{56}Ni and ejecta mass distributions are investigated. The conclusions are summarized in Section 8.

2 DATA COLLECTION, REDUCTION, AND CALIBRATION

The SNe, listed in Table 1, were discovered by a variety of different sources over 5 years. Subsequent observations were obtained from various locations and instruments, as follows:

(i) The 3.6 m ESO New Technology Telescope (NTT) at La Silla, Chile, using the ESO Faint Object Spectrograph and Camera (v.2) (EFOSC2) for both spectroscopy and *BVRI* imaging.

(ii) The 2.0 m Liverpool Telescope (LT; Steele et al. 2004) at the Roque de los Muchachos Observatory, La Palma, Spain. *BVugriz* photometric data were obtained using IO:O, while spectroscopic

Table 1. General information on the SNe, host galaxies, and reddening.

SN	Type	α (J2000)	δ	Gal type[a]	z	μ [mag]	$E(B-V)_{MW}$ [mag]	$E(B-V)_{host}$ [mag]
2013F	Ic-6	25:48:25.03	−41:19:56.21	SABbc	0.005	31.29	0.018	1.4 ± 0.2
2013bb	IIb(I)	14:12:13.96	+ 15:50:31.49	SAB(s)bc	0.018	34.52	0.014	0.3 ± 0.1
2013ek	Ib	20:57:53.90	−51:52:24.49	SBc	0.016	33.50	0.033	0.04 ± 0.01
2015ah	Ib	23:00:24.63	+ 01:37:36.80	SABcd	0.016	33.86	0.071	0.02 ± 0.01
2015ap	Ib	02:05:13.32	+ 06:06:08.39	SBd	0.011	33.27	0.037	negligible
2016P	Ic-6∗	13:57:31.10	+ 06:05:51.00	SBbc	0.015	34.17	0.024	0.05 ± 0.02
2016frp	Ib	00:21:32.54	−05:57:24.29	–	0.027	35.23	0.031	negligible
2016gkg	IIb	01:34:14.46	−29:26:25.00	SB(rs)bc	0.005	31.22	0.017	0.05 ± 0.02
2016iae	Ic-7	04:12:05.53	−32:51:44.75	SBb pec	0.004	31.19	0.014	0.65 ± 0.2
2016jdw†	Ib	13:16:19.62	+ 30:40:32.67	–	0.019	34.66	0.01	negligible
2017bgu†	Ib	16:55:59.47	+ 42:33:36.01	–	0.009	33.20	0.029	0.02 ± 0.01
2017dcc	Ic-3	12:49:04.89	−12:12:22.42	–	0.025	35.06	0.041	negligible
2017gpn†	IIb(I)	03:37:45.26	+ 72:31:58.70	SAB(s)b: pec	0.007	32.60	0.3	negligible
2017hyh	IIb(I)	07:10:41.07	+ 06:27:41.40	–	0.012	33.54	0.118	0.04 ± 0.01
2017ifh†	Ic-4	06:35:03.56	+ 50:26:27.90	–	0.039	35.97	0.117	0.05 ± 0.02
2017ixz	IIb	07:47:03.03	+ 26:46:25.77	–	0.024	34.98	0.033	negligible
2018ie†	Ic-4	10:54:01.06	−16:01:21.40	SB(rs)c	0.014	33.35	0.06	0.02 ± 0.01
2018cbz†	Ic-4∗	13:41:18.61	−04:20:46.54	SBd	0.022	35.03	0.03	0.03 ± 0.025

Notes. [a]See Appendix for discussion on some of the host environments.

∗Ambiguous classification.

†Observed independently of PESSTO/ePESSTO.

data were collected using the Spectrograph for the Rapid Acquisition of Transients (SPRAT; Piascik et al. 2014).

(iii) The Las Cumbres Observatory (LCO; Brown et al. 2013) network of robotic telescopes. Spectroscopy was obtained using the Floyds spectrographs and $BVg_pr_pi_p$ imaging from the Spectral cameras on the LCO 2.0 m telescopes at Hawaii and the Siding Spring Observatory. Photometry was also obtained from the 1 m telescopes at the McDonald Observatory, the Cerro Tololo Inter-American Observatory (CTIO), and the South African Astronomical Observatory (SAAO).

(iv) Near-infrared *JHK* imaging from NOTcam on the Nordic Optical Telescope (NOT), operated by the Nordic Optical Telescope Scientific Association at the Observatorio del Roque de los Muchachos.

(i) The Gamma-Ray Burst Optical/Near-Infrared Detector (GROND; Greiner et al. 2008), a 7-channel imager that collects multicolour photometry simultaneously with $g'r'i'z'JHK_s$ bands, mounted at the 2.2 m MPG telescope at ESO La Silla Observatory in Chile.

(ii) The twin ATLAS 0.5 m telescope system based on the Haleakala and Mauna Loa, Hawaii, USA (Tonry et al. 2018). The ATLAS *c* and *o* filters are approximately $g + r$ and $r + i$, respectively.

(iii) The Wide-field Spectrograph (WiFeS) on the Australian National University 2.3 m telescope at the Siding Spring Observatory (on behalf of PESSTO).

(iv) Images were acquired with the g' filter mounted on the 60 cm PROMPT3 telescope (pixel size of 1.4") and with the Luminance filter mounted on the 80 cm PROMPT7 telescope (pixel size of 0.66"). Both telescopes are located at Cerro Tololo Inter-American (CTIO) observatory, Chile. Observations by the Chilean Automatic Supernova Search (CHASE; Pignata et al. 2009).

(v) *BVRI* photometry using the ANDICAM-CCD on the SMARTS 1.3 m CTIO observatory, Chile.

(vi) The Deep Imaging Multi-Object Spectrograph (DEIMOS; Faber et al. 2003) on the W. M. Keck Observatory, Haleakala, as part of LCO Supernova Key Project

Alignment, stacking, aperture photometry, and calibration of the LT, LCO, NTT, and SMARTS imaging to the Sloan Digital Sky Survey (SDSS; Eisenstein et al. 2011) and the American Association of Variable Star Observers Photometric All-Sky Survey (APASS) standard stars in the field was achieved using the IRAF DAOPHOT package and a custom PYTHON script. NOTCam reductions (differential flat-fielding, sky subtraction, distortion correction, and stacking of dithered images) were done using a modified version of an external IRAF package notcam (v 2.5).[1] *JHK* bands were calibrated to Two Micron All-Sky Survey (2MASS; Skrutskie et al. 2006) sources in the field. GROND images were reduced by the GROND pipeline (Krühler et al. 2008), which applies de-bias and flat-field corrections, stacks images, and provides astrometric calibration. NTT spectra were reduced via a custom pipeline as described in Smartt et al. 2015. SPRAT spectra were reduced and calibrated in wavelength via the pipeline described in Piascik et al. (2014) and Barnsley, Smith & Steele (2012), and calibrated in flux via a custom PYTHON pipeline. WiFeS spectral reduction is described in Childress et al. (2016).

The filters used on the LT, GROND, and LCO telescopes are all subtly different, as demonstrated in Fig. 1. For the most part, effects are small but most pronounced for the GROND g' filter ($\lambda_{eff} \sim 4505$ Å) which is bluer than the IO:O SDSS-*g* filter ($\lambda_{eff} \sim 4696$ Å) and so probes an area of the spectrum closer to the *B*-band ($\lambda_{eff} \sim 4348$ Å). This leads to a clear difference in the light curves of GROND-g' and the other *g* filters. Each band is treated independently throughout.

---

[1]http://www.not.iac.es/instruments/notcam/guide/observe.html#reductions
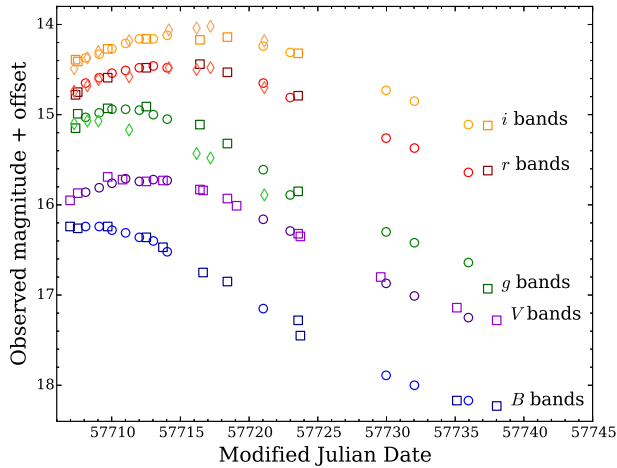
Figure 1. A comparison of the effects of different filter responses on the early-time light curve of SN 2016iae; LT (circles), GROND (diamonds), LCO (squares).

2.1 Host galaxy distances and reddening

Distances are taken from the NASA Extragalactic Database[2] (NED) and assume a cosmology of $H_0 = 73$ km s^{-1} Mpc^{-1}, $\Omega_m = 0.27$, $\Omega_\Lambda = 0.73$ throughout. Distances to objects outside of the Hubble flow can be highly uncertain; however, our error calculations carry no uncertainty for μ. This is to allow the photometric properties calculated in this work, and their associated errors, to be easily projected to different distances.

Galactic reddening $E(B - V)_{MW}$ for each object is found in Schlafly & Finkbeiner (2011). Host reddening $E(B - V)_{host}$ is estimated using the equivalent width of the host–galaxy Na I D doublet absorption feature in the spectra (Poznanski, Prochaska & Bloom 2012), although there are limitations to this method when applied to low-resolution spectra (Poznanski et al. 2011). The equivalent width of the Na I D line is calculated in relation to a 'local continuum', defined as the boundaries of the Na I absorption line. While it is found that *S/N* and the estimated local continuum affect the value of the equivalent width, the largest contribution to the error is the uncertainties given in Poznanski et al. (2012). This method also assumes a Milky Way type extinction law with $R_V = 3.1$, which does not necessarily apply to other galaxies (e.g. M82; Ashall et al. 2014). Also, the equations used to derive $E(B - V)_{host}$ are very sensitive to the equivalent width and when the lines saturate the relationship is no longer valid. Other methods of deriving $E(B - V)_{host}$ use colours to estimate the reddening (Drout et al. 2011; Stritzinger et al. 2018b). These methods are not used here, but tests of various SNe show that they broadly agree.

3 LIGHT CURVES

3.1 Multicolour light curves

The multicolour light curves for each SN are shown in Fig. 2, with the photometry listed in Table 2.

The light curve of type IIb SN 2016gkg (Tartaglia et al. 2017; Arcavi et al. 2017; Bersten et al. 2018) shows a very clear shock-cooling tail, which is characteristic of many SNe IIb with extended envelopes (e.g. SN 1993J, SN 2011fu, SN 2013df; Richmond et al.

1994; Kumar et al. 2013; Morales-Garoffolo et al. 2014). The ATLAS light curve of the type IIb SN 2017ixz suggests that a shock cooling tail is detected, with a 1 mag decline in 4 days before the light curve rises (there is a robust non-detection at $o = 20$ mag just two days before the first point). We have no indication of shock cooling in other H-rich SNe, although the data sampling is insufficient to constrain this quantitatively.

3.2 Bolometric light curves

Optical 4000–10000 Å (pseudo-)bolometric light curves are constructed by converting the de-reddened apparent magnitudes to monochromatic fluxes, using the extinction law given in Cardelli, Clayton & Mathis (1989) and zero-points from Fukugita et al. (1996), and then integrating the resulting spectral energy distribution over the wavelength range. The bolometric flux is then converted to bolometric luminosity using the distance modulus given in Table 1. The resulting light curves are shown in Fig. 3 and compared with the sample from Prentice et al. (2016), hereafter P16.

3.2.1 Measuring physical parameters

Light-curve properties are derived using a low (3-5) spline from UNIVARIATESPLINE, part of SCIPY. The peak luminosity L_p is measured, plus three characteristic time-scales; $t_{-1/2}$, $t_{+1/2}$, and δm_{100}.

The time-scales $t_{-1/2}$ and $t_{+1/2}$ are the times taken for the light curve to rise from $L_p/2$ to L_p and decay from L_p to $L_p/2$, respectively. Uncertainties for these two values incorporate the errors on the spline fit, the photometric calibration, and $E(B - V)_{tot}$. The linear decay rate at 100 days, δm_{100}, in units of mag d^{-1}, is measured via a linear fit through the light curve over several tens of days around, or as close as possible to, 100 days past maximum when the SN is on the ^{56}Co tail.[3] If the quality of the photometric data is good then the error on this value is negligible as given by the standard deviation of the covariance matrix used in the least fitting. The goodness of fit is also tested by changing the range of time over which the function was applied; however, it was found that the maximum deviation was a thousandth of a magnitude per day and typically lower. At this phase, the mass of ^{56}Ni synthesized during explosive silicon burning, and the deposition energy from the decay products (positrons and γ-rays) of ^{56}Co into the optically thin ejecta is probed. Full trapping of γ-rays would result in a decline of 0.0098 mag d^{-1} and a decline rate greater than this indicates less efficient trapping of the ^{56}Co decay products. On the other hand, a slower decay rate suggests some different powering source (as was the case for iPTF15dtg; Taddia et al. 2018a) All temporal parameters are measured in the supernova rest-frame. The results are given in Table 3 and discussed further in Section 5.

3.2.2 Light curave modelling, ^{56}Ni mass, and rise time

The time taken for the light curve to rise from explosion to maximum light t_p is used to derive the ^{56}Ni mass (M_{Ni}) synthesized during the explosion, but unfortunately this value is seldom known accurately. Estimates can be made by fitting a simple quadratic to the *SN* light curve on the rise but this method requires a well-sampled rise. Alternatively, a robust non-detection shortly before discovery can help constrain the explosion date.

[2]https://ned.ipac.caltech.edu/

[3]$\tau_{1/2}(^{56}$Co$) = 77.27$ days
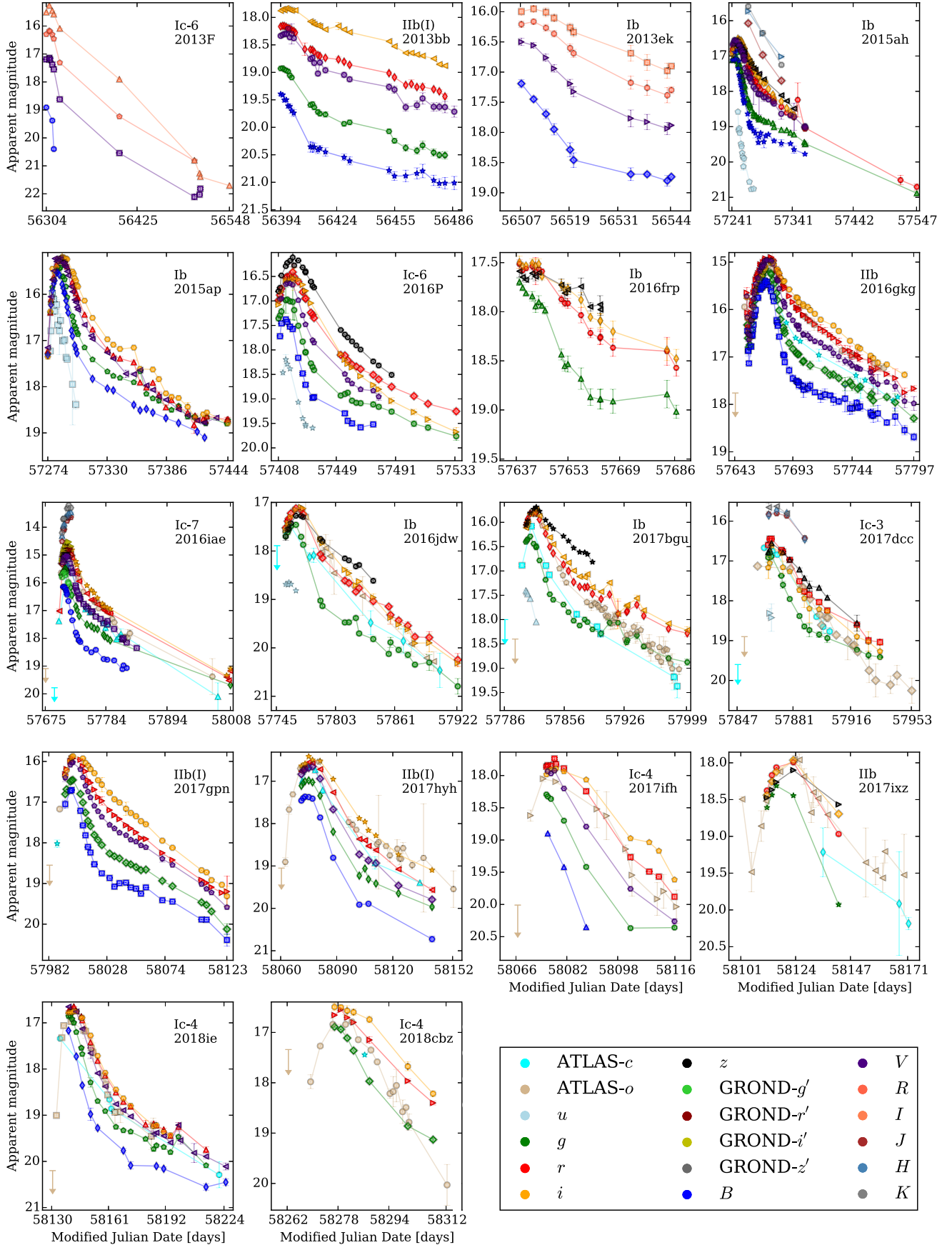
Figure 2. The observed multicolour light curves of the SNe in the sample. For clarity, similar bands (e.g. *g* and g_p) have been grouped together despite subtle differences in filter response functions.

Table 2. Table of photometry.

SN	MJD	band	mag	Facility
2013F	56304.08	B	18.91 ± 0.05	NTT
2013F	56312.04	B	19.38 ± 0.05	NTT
2013F	56314.05	B	20.40 ± 0.05	NTT
2013F	56304.08	V	17.19 ± 0.05	NTT
2013F	56312.04	V	17.37 ± 0.02	NTT

Note. The full table can be found in machine-readable format online.

To overcome this limitation and estimate t_p for all SNe, the pseudo-bolometric light curves are fit with the analytical model of Arnett (1982), as formulated for the photospheric phase in Valenti et al. (2008b). This model assumes homologous expansion, spherical symmetry, constant opacity, full γ-ray trapping, and that ^{56}Ni is located centrally. The light-curve model was fit to the data using a Monte Carlo routine that allowed the time of explosion t_{exp}, the characteristic time scale of the light-curve model τ_m, and M_{Ni} to vary. The explosion time t_{exp} was not allowed to take a value that is after the date of discovery, nor was the model light curve allowed to exceed the limit set by any earlier non-detection. Information on discovery dates and corresponding photometry was found via Bright Supernova[4] (Gal-Yam et al. 2013).

The model fits were found to be reasonable but not perfect, and the relationship between τ_m and t_p is complex. The 'best fit' models to early data tended to underestimate the rise time indicated by the underlying data, by a couple of days. By forcing the model to include more post-max data points, the peak of the model could be matched with the peak of the data, at the expense of the quality of fit. Given this uncertainty, we make the assumption that τ_m and t_p are approximately equivalent, with the value being the average of the best fit and forced peak fit to the data. Finally, δM_{Ni} is calculated from δL_p and δt_p using the formulation in Stritzinger & Leibundgut (2005). We find M_{Ni} values in the range 0.026–0.19 $M_\odot$, with t_p between 7.8 and 20.7 d (see Table 3). M_{Ni} is discussed in relation to other events in Section 6.1.

3.2.3 Estimating ejecta mass

The ejecta mass M_{ej} of the supernova is estimated through the following relation:

$$M_{ej} = \frac{1}{2}\left(\frac{\beta c}{\kappa}\right)\tau m^2 v_{sc}. \qquad (1)$$

Here, $\beta \approx 13.7$ is a constant of integration, κ is the opacity of the ejecta, and v_{sc} is a 'characteristic' velocity of the ejecta. When applied to this model, κ is often taken to be constant with a value between 0.07 and 0.1 cm^2 g^{-1}, but in reality is variable throughout the SN ejecta (see Nagy 2018). Additionally, defining a 'typical' velocity in the form of v_{sc} is difficult, as the ejecta has a continuous velocity profile. v_{sc} is commonly taken to be the photospheric velocity, v_{ph}, at maximum light or some estimated expansion velocity. M_{ej} is estimated here by using $\tau_m = t_p$, assuming that $\kappa = 0.07$ cm^2 g^{-1} (see Taddia et al. 2018b), and that the scale velocity is given by the lowest measurable line velocity at maximum light. In the case of He-poor SNe, this is Si II λ 6355, while for He-rich SNe it is O I λ 7774 if present or He–I λ 5876 if not.

The resulting values for t_p, M_{Ni}, v_{ph}, and M_{ej} are given in Table 3. M_{ej} is given as an absolute value because the true uncertainty

associated with this is unquantifiable (we do not know how accurate – or wrong – a 1D model is). Equation (1) is most sensitive to the value of t_p, such that an uncertainty of ± 2 days leads to variations of $\sim\pm 30$ per cent in M_{ej}, but the presence of an uncertainty in the calculation may lead to undue confidence in the result. The results are discussed in the context of other SE–SNe in Section 6.2. We note here that our derived ejecta masses are between 1.2 and 4.8 $M_\odot$ and our sample contains the most massive H-rich SE–SNe to date; SN 2013bb.

3.3 Temperature evolution

The temperature evolution of each SN during the photospheric phase was calculated by converting the de-reddened multicolour photometry to monochromatic fluxes and constructing rest-frame SEDs. A Monte Carlo code was then used to fit the spectral energy distributions (SEDs) with a Planck function to find the best-fit temperature. Errors on the fit are calculated by allowing the flux at the beginning of each run randomly to take different values within the range of photometric errors. Variation due to uncertainty in $E(B - V)_{tot}$ was calculated and found to be within the MC-derived uncertainties, with the exception of SNe 2016iae and 2013F where $\delta E(B - V)_{host}$ is large. Here the temperature errors can be ± 25 per cent a week before maximum light, falling to ± 8 per cent at $+ 20$ d. Because uncertainty in $E(B - V)$ does not act randomly (i.e. lower $E(B - V)$ reduces all the temperature measurements) this contribution is not included in the plotted error bars. Additionally, if spectra exist more than 1.5 d before the first photometric observation, then a Planck function was fit to these to estimate the earliest temperature. For SN 2017ixz (Jones et al. 2017) and SN 2018ie (Lin et al. 2018), this necessitated the use of classification spectra.

The temperature evolution of most SNe for the time observed is quite similar (Fig. 4); an initial cooling phase with $T(t_{max}) = 4000 - 8000$ K, levelling off to ~ 5000 K around 7–10 days after maximum light. The apparent rise in temperature after this is unlikely to be real however, as this epoch is defined by deviation from a thermal spectrum (i.e. emission lines begin to show) and a loss of the photosphere.

The H-rich SNe show a series of different behaviours. The most He-rich of these, SNe 2016gkg and 2017ixz, both had shock-cooling tails, and both had rise times of $t_p \sim 20$ d. The shock-cooling phase of SN 2016gkg is reflected in the temperature evolution showing a double-peaked profile, with the second peak occurring approximately 5 days before t_{max}. SN 2017ixz does not show this behaviour, with the temperature ~ 7 d after t_{exp} already being in decline. The type IIb(I) SN 2017gpn may have a secondary peak, but as the early phase of this SN was not observed in multicolour photometry it is not possible to tell conclusively. The ATLAS-o detection suggests there was no prominent shock-cooling tail. Finally, the unusual SN 2013bb is rather cool in comparison, with $T \sim 6200$ K approximately 9 days before maximum light.

The He-rich SN 2015ap was discovered early, allowing us to constrain the explosion date to within a couple of days. The first temperature estimate is approximately 2 d after explosion and is around 11000 K. The variation in the temperature curve may just reflect photometric errors; however, the flattening at ~ 9000 K between -10 and 0 d may be real (a blackbody fit to spectra taken -5 d gives $T \sim 8500$ K). SN 2016frp remains hotter than the other SNe after t_{max}, as is apparent at $+15$ d when the temperature of the SN is 1000 K higher than the rest. SNe 2016jdw and 2017bgu have comparatively long rise times (~ 19 and 18 days respectively)
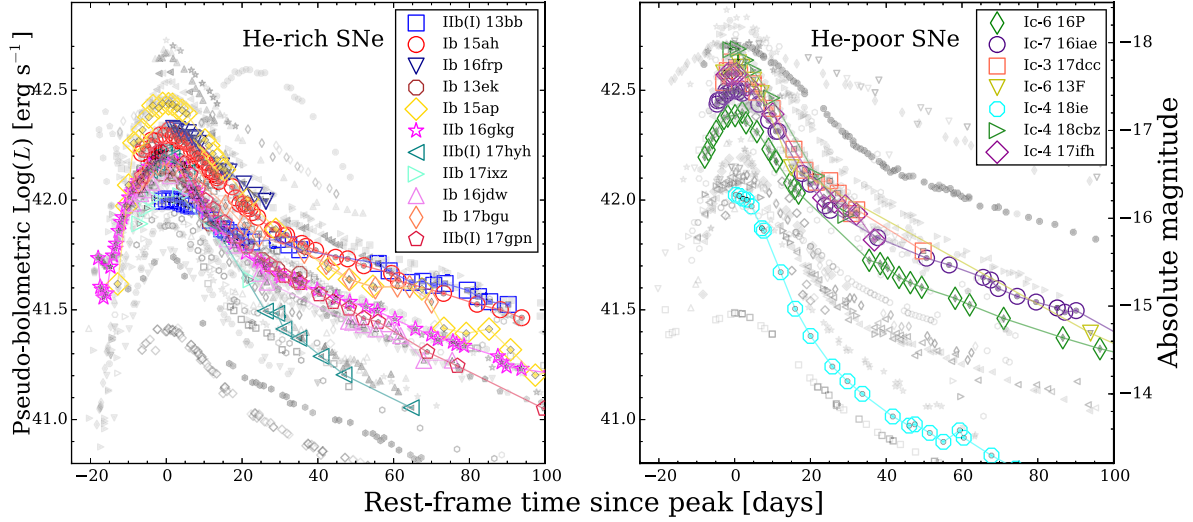
Figure 3. The 4000–10000 Å pseudo-bolometric light curves for (left) He-rich SNe and (right) He-poor SNe compared with the sample of P16 (grey). Note the shallow light curve of SN 2013bb. Grey open markers denote SNe for which the host extinction is unknown.

Table 3. Statistics derived from the 4000–10 000 Å bolometric light curves.

SN	$\log(L_p)$ [erg s^{-1}]	$t_{-1/2}$ [d]	$t_{+1/2}$ [d]	δm_{100}^a [mag d^{-1}]	t_p [d]	M_{Ni} [M$_\odot$]	$v_{ph}(t_{max})$ [km s^{-1}]	M_{ej}^b [M$_\odot$]
2013F	42.6 ± 0.2	–	11.5 ± 0.1	–	12 ± 1	$0.15 \pm_{0.06}^{0.09}$	9000	1.4
2013bb	42.0 ± 0.1	–	56 ± 10	0.011(1)	$\sim 25^c$	0.07 ± 0.02	7000	4.8
2013ek	42.13 ± 0.02	–	15.0 ± 0.7	–	13 ± 2	0.05 ± 0.01	6000	1.2
2015ah	42.29 ± 0.01	–	19.3 ± 0.2	0.014(1)	16 ± 1	0.092 ± 0.007	7000	2.0
2015ap	42.50 ± 0.03	8.0 ± 0.2	14.2 ± 0.2	0.020(1)	13.5 ± 1.0	0.12 ± 0.02	9000	1.8
2016P	42.39 ± 0.02	9.9 ± 0.4	13.9 ± 0.2	0.014(1)	14 ± 1	0.09 ± 0.02	7000	1.5
2016frp	42.32 ± 0.01	9 ± 1	21.6 ± 0.7	–	16 ± 1	0.08 ± 0.007	9000	2.5
2016gkg	42.19 ± 0.03	11.6 ± 0.6	20.4 ± 0.2	0.018(1)	20.7 ± 0.5	0.085 ± 0.008	8000	3.7^d
2016iae	42.4 ± 0.2	8.2 ± 0.1	15.2 ± 0.1	0.018(1)	15 ± 1	$0.13 \pm_{0.05}^{0.08}$	9000	2.2
2016jdw	42.08 ± 0.04	12 ± 2	17.1 ± 0.5	0.018(2)	19 ± 1	0.06 ± 0.02	11000	4.3
2017bgu	42.16 ± 0.02	–	22.5 ± 0.6	0.016(2)	18 ± 1	0.069 ± 0.003	8500	2.9
2017dcc	42.6 ± 0.1	8 ± 1	15.5 ± 0.5	–	15 ± 1	0.16 ± 0.04	13000	3.1
2017gpn	42.23 ± 0.02	9.9 ± 0.1	17.3 ± 0.3	0.023(1)	15 ± 1	0.070 ± 0.007	8000	2.0
2017hyh	42.20 ± 0.01	8 ± 1	13.0 ± 0.1	0.029(1)	16 ± 1	0.069 ± 0.005	11000	3.0
2017ifh	42.6 ± 0.1	9 ± 1^e	14.7 ± 0.3	–	13 ± 2	0.16 ± 0.01	16000	3.0
2017ixz	42.02 ± 0.02	9 ± 1^e	–	–	20.0 ± 0.5	0.056 ± 0.03	8000	3.5
2018ie	42.02 ± 0.01	5.0 ± 0.5^e	10.1 ± 0.5	–	7.8 ± 0.5	0.026 ± 0.002	23000	1.5
2018cbz	42.69 ± 0.03	8 ± 1^e	–	–	14 ± 2	0.19 ± 0.04	14000	3.0

Notes. ^{a}Uncertainty of last digit given in parentheses. ^{b}See text for a discussion on the uncertainty in M_{ej}.
^{c}From Karamehmetoglu et al. (in prep.). ^{d}Bersten et al. (2018) calculate $M_{ej} \sim 3.4$ M$_\odot$. ^{e}Estimated from ATLAS photometry.
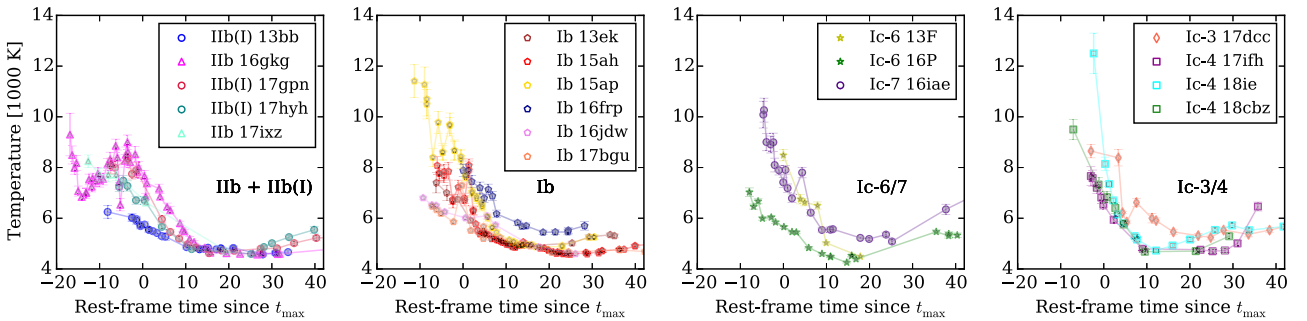
Figure 4. The temperature evolution of the SNe with respect to t_{max} for H/He-rich SNe (top left), H-poor/He-rich SNe (top right), narrow lined He-poor SNe (lower left), and broad-lined SNe Ic (lower right).

and this is reflected in their temperature evolution. By the time of the first multicolour observations, they are already cooler and their temperature curves evolve more slowly than the other SNe Ib.

Of the SNe Ic-6/7, SN 2016P is apparently cooler than both SNe 2016iae and 2013F, and although the latter are affected by significant and uncertain $E(B - V)_{host}$, accounting for this uncertainty still places them above SN 2016P before +10 d. Its temperature evolution has more in common with type Ib SNe 2016jdw and 2017bgu. A check against blackbody fits to the maximum light spectrum shows that $T = 8000$ K fits the continuum well, but overestimates the location of the peak. A temperature of $T = 6000$ K matches the peak of the spectrum (and the SEDs) but not the continuum.

For SNe Ic-3/4, attempts to calculate T are complicated due to a combination of line blanketing and extended line-forming regions, which are seen as broad absorption regions. Here, flux in the near-UV is scattered to progressively redder wavelengths, finally escaping through 'windows' of lower opacity which manifest themselves in the spectra as pseudo-emission peaks. As a result, the spectra and SEDs may not be well represented by a blackbody as the flux peak is not representative of T. Examination of T derived from SEDs and spectra for the ePESSTO SN in this subgroup, SN 2017dcc, reveals a similar issue to SN 2016P. T estimates derived from SED fits and spectral continuum fits (>5000 Å) are in agreement, but these temperatures fail to match the shape of the spectrum in the blue. This would be consistent with flux redistribution however, and under this assumption, these SNe show similar temperature and evolution around maximum light. SN 2018ie is initially very hot some ∼3 days after explosion (see ATLAS limits) and undergoes rapid cooling and remains comparatively hot after t_{max}. Note, that despite similar issues between SN 2016P and the Ic-3/4 SNe in terms of calculating T, SN 2016P is much cooler. The classification of SN 2016P is ambiguous; it was originally classified as a 'Ic-BL' (Zhang & Wang 2016), but the spectra are heavily contaminated by host–galaxy emission lines. Its spectral properties (velocities, shape) better fit SNe Ic-6/7, yet in this instance it better matches the broad-lined SNe. The temperature evolution of the SNe presented here is consistent with that found by Taddia et al. (2018b).

4 SPECTROSCOPY

The maximum light spectra of the 18 SNe are shown in the top panel of Fig. 5; plots of all spectra can be found in the supplementary material. Spectra not already released as part of a PESSTO data release will be uploaded to WISeREP[5] (Yaron & Gal-Yam 2012). Eight of the SNe were observed as they entered the nebular phase (Fig. 6). They show emission lines common to H-deficient core-collapse supernova, such as a series of Fe II lines at ∼5000 Å, Na I D, O I λλ7772, 7774, 7775 and the Ca II NIR triplet during the first month after explosion, and [O I] λλ 6300, 6363, [Ca II] λλ 7292, 7324 during the nebular phase.

4.1 Measuring line velocities

For all SNe, line velocities of common elements (e.g. H, He, Si, Fe, O, Ca, and Na) are calculated by measuring the minimum of the absorption profile in velocity-space relative to the rest position of the ion. The error on this value is calculated by taking the width δv in velocity space of the minimum, where $df_\lambda(v)/dv \sim 0$. It is

important to note that for blended lines (e.g. those in SNe Ic-3 and 4) the absorption minimum does not necessarily reflect any single Doppler-shifted atomic transition (Prentice & Mazzali 2017), and the uncertainty represents the entire width of the feature. This approach results in very conservative errors.

The line velocities of the SN are measured during the photospheric phase (<30 d after t_{max}). For the H-rich SNe, we measure the velocity as defined by the minima of the absorption profiles of H α, He I λ 5876, Fe II λ 5169, O I λ 7774, and the Ca II NIR triplet. For the He-poor SNe we measure Fe II, O I, and Ca II as before, and further include Na I D and Si II λ 6355. The line velocity plots are shown in Fig. 7. It can be seen that Ic-4 SN 2018ie has the highest line velocities of any object in this sample.

4.1.1 Hα

The H α velocities of the H-rich SNe show two contrasting behaviours. SNe 2016gkg, 2017gpn, 2017ixz, and 2013bb show similar velocity evolution, at least where the data overlap in time. However, SN 2017hyh has high velocity H α that declines in velocity rapidly, by ∼6000 km s^{-1} over 20 days and has a velocity ∼17 000 km s^{-1} at t_{max}. At this epoch, it is the highest velocity H-rich SE–SN known (Liu et al. 2016; Prentice & Mazzali 2017). Interestingly, this shows similarity to the H α velocity curves of the SNe Ib and those of Si II in He-poor SNe. The H α line in SNe Ib declines rapidly to peak and usually disappears approximately a week later. While the presence of H in SN 2017hyh is clear, the identification of this line in SNe Ib is ambiguous. It may be Si II or a mix of this line with H α, but the behaviour here suggests that as the SN approaches peak the line is dominated by the Si II component. The solution to this problem will require non-LTE spectral modelling.

4.1.2 He I λ 5876

Both SNe 2015ap and 2016jdw are towards the upper end of the SN Ib He I λ5876 velocity distribution (see Liu et al. 2016; Prentice & Mazzali 2017; Fremling et al. 2018). A curious behaviour is seen in the He I velocity of SN 2015ah which increases towards t_{max}. This behaviour is unusual, as post-max increases in He I λ5876 velocities have been seen before (e.g. SN 2005bf) but never on the rise. Further analysis suggests that this only occurs in the He I λ 5876 line, and not in the other He I lines. This could be interpreted as the feature being a Na I D/He I blend, and the evolution being due to changing line strength; however, the feature is no stronger or broader than in other SNe Ib where this effect is not seen.

4.1.3 Fe II λ 5169

The high-velocity nature of SN 2017hyh is again apparent in the Fe II velocity curves, although post-maximum measurements are prevented by the poor S/N of the spectra. Unfortunately, no measurement of the Fe II velocity in SN 2015ap could be made due to contamination by host galaxy lines. The velocity curve of SN Ic-7 2016iae is rather flat, as was noticed for Ic-7 SN 2007gr (Valenti et al. 2008a), which is again further evidence for the ejecta of these SNe having a steep density profile. The remainder of the SNe show velocity curves that decrease rapidly during the photospheric phase, and this occurs most rapidly in the Ic-3/4 SNe. These latter SNe have the highest line velocities here (but see the previous caveat on measuring velocities from broad lines).
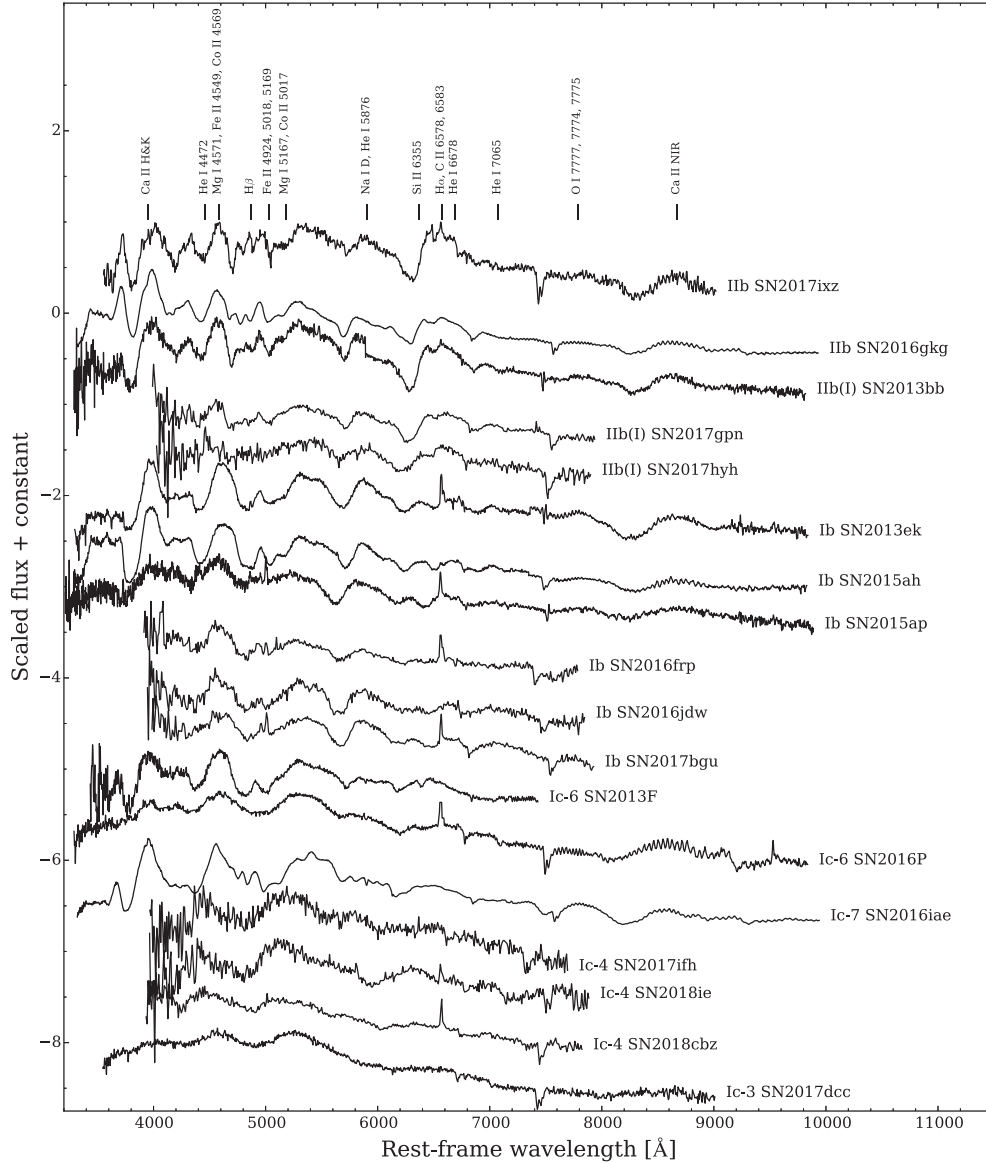
Figure 5. t_{max} spectra of the 18 SE-SNe grouped according to sub-type. Prominent galaxy lines have been truncated in SNe 2016frp and 2016P, these greatly affect the appearance of the latter around 5000 Å. Plots of all the spectra can be found in the supplementary material.

4.1.4 Na I D

The only velocity that could clearly be measured for Ic-6 SN 2016P is Na I D. It shows a velocity curve similar in shape to Ic-7 SN 2016iae but at a higher velocity. As a contrast, the two measured velocities for Ic-6 SN 2013F are much lower, which was also reflected in the Fe II velocities.

4.1.5 Si II λ 6355

As with Na I, Si II is measured in He-poor SNe only. The behaviour of the velocity curves was discussed in relation to H α. However, SN 2016iae and SN 2013F again show the velocity difference seen in Na I. The measurements of SN 2016P are not robust, although if the line is present and not an artefact of the host emission lines then the velocities can be considered as upper limits. Clearly, this is hard to reconcile with the Na I velocities. The SN Ic-3/4 velocities

are again much higher than for any other SN type and also decline far more rapidly.

4.1.6 O I λ 7774

The O I line can be hard to measure due to a strong telluric feature that tends to lie at 8000–10000 km s^{-1} from its rest wavelength in low-z SNe. The best sampled velocity curve is that of SN 2016iae which displays an almost linear decline. We also measure an exceptionally high velocity for SN 2018ie ($\sim$25000 km s^{-1}). The remaining measurements are hindered by large uncertainties but show that the O I velocity in He-rich SNe varies significantly, more so than for H α or He I.

4.1.7 Ca II NIR

The Ca II NIR absorption feature can be easy to measure if the spectra extend sufficiently redward, but uncertainty in its measure-
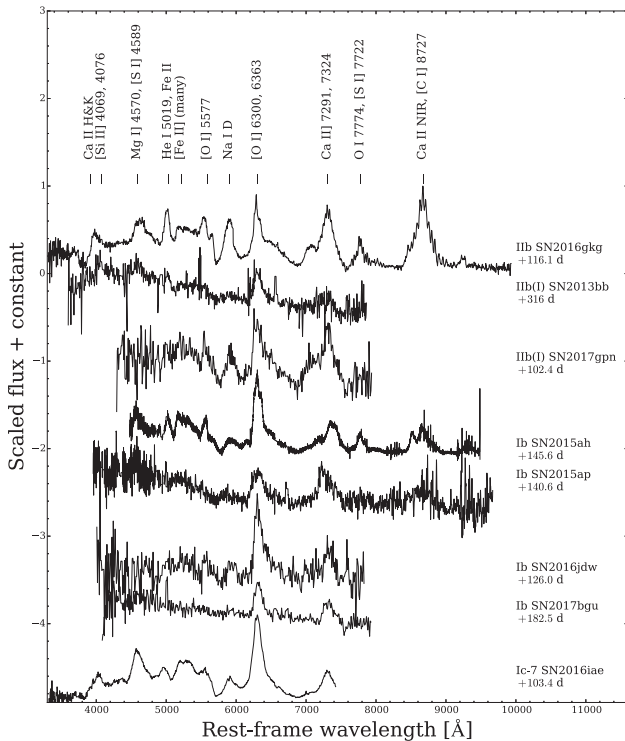
Figure 6. Nebular phase spectra of 8 SE–SNe, where galaxy lines have been truncated. Common emission lines associated with the nebular phase of core-collapse SNe are shown. Notice that even in H-rich SE–SNe, there is no clear Hα emission during this phase.

ment can come from the broad nature of the feature, and the wide wavelength separation of the triplet components (8498 Å, 8542 Å, and 8662 Å), which means that the actual velocity is poorly constrained. Velocities determined from Ca II NIR in SN 2015ah decrease rapidly, with no clear indication of levelling off (compare this with the other SNe). This behaviour was also present in all the other velocities that could be measured for SN 2015ah except for He I. This makes the evolution of the He I λ 5876 line even more exceptional. The velocity curve of SN 2016iae is again found to be flat, while the velocity of SN 2016P is high initially before falling below that of SN 2016iae. Finally, a single measurement of SN 2017hyh confirms its high velocity nature in relation to He-rich SNe.

4.2 Luminosity of [O I] λ 6300 and progenitor M_{ZAMS}

Oxygen is an effective coolant of the SN ejecta at late times. The luminosity of the [O I] λ 6300 line, $L_{[OI]}$, was calculated by absolute calibration in flux of the nebular spectra to the available R/r −band photometry, correcting for $E(B − V)_{MW}$ then correcting for the effects of cosmological expansion, then correcting for $E(B − V)_{host}$. Under the assumption that the emitting region is spherical, a single Gaussian profile was fit to the spectra centred on 6300 Å and was allowed to extend to a width that remained inside the emission line. This approach was taken to avoid including emission from other lines in the region. A pseudo-continuum, defined from some featureless region close to 6000 Å, was subtracted from the Gaussian flux. The Gaussian flux density was integrated over the wavelength region 6137–6518 Å (regions where $f_{continuum} > f_{Gaussian}$ were treated as zero) and the integrated flux converted to luminosity

using the distance modulus. Errors are assessed by allowing the position of the pseudo-continuum to vary between ±10 Å from the reference position. This uncertainty was then added in quadrature to the uncertainty on the flux due to photometric errors.

The flux is then normalized to the energy decay rate of ^{56}Co following the procedure of Jerkstrand et al. (2015)

$$L_{norm}(t) = \frac{L_{[OI]6300}}{1.06 \times 10^{42} \frac{M_{Ni}}{0.075 M_\odot} (e^{\frac{-t}{111.4d}} - e^{\frac{-t}{8.8d}}) \text{ erg sec}^{-1}} \quad (2)$$

The results are shown in Fig. 8, and we note that L_{norm} follows the behaviour of $L_{[OI]}$. For Ic-7 SN 2016iae, L_{norm} increases between ∼120 and 160 d. The oxygen luminosity of type Ib SN 2016jdw remains above that of the other SNe, by nearly 100 per cent in some cases. The late time photometry of SN 2013bb was estimated from EFOSC2 images to be $r \sim 21.5$ mag at ∼ 314 d after explosion.

Jerkstrand et al. (2015) used L_{norm} to estimate the M_{ZAMS} of the progenitor stars of several SNe IIb, under the assumption that it provides a good measurement of the He-core mass, which can be linked to M_{ZAMS} (this is model dependent, but to less than a factor of 2; Jerkstrand et al. 2014). They compared the L_{norm} curve with models ranging from $M_{ZAMS} =12–17$ M$_\odot$, which contained oxygen masses of $M_O = 0.3–1.3$ M$_\odot$. Comparison with their Figure 15 shows that SNe 2015ap and 2017gpn are within the range of models for which $M_{ZAMS} =12–13$ M$_\odot$. The progenitors of SNe 2015ah and 2016gkg lies between $M_{ZAMS} =13–17$ M$_\odot$, but appear closer to the lower values. The estimated initial mass of the progenitor of SN 2016gkg is within the range calculated in other works (15-20 M$_\odot$; Kilpatrick et al. 2017; Tartaglia et al. 2017) and sits at the same position as SN 2008ax in Jerkstrand et al. (2015). For SNe 2013bb, 2016iae, 2016jdw, and 2017bgu the progenitors may have initial masses around 17 M$_\odot$. Their L_{norm} curves are close to the 17 M$_\odot$ model, and O production increases strongly with progenitor mass over 16 M$_\odot$ (Jerkstrand et al. 2015). Note that these values are based upon M_{Ni} calculated from the 4000–10000 Å bolometric light curve, which underestimates the peak luminosity by ∼30 per cent (P16) and would reduce the estimated M_{ZAMS}.

## 5 COMPARISON OF PHYSICAL PROPERTIES WITH OTHER SE-SNE

The properties of the 18 SNe can be compared with those found in larger samples. In particular, we can examine how they fit within the distributions of $\log_{10}(L_p)$ (hereafter $\log(L_p)$), $t_{-1/2}$, $t_{+1/2}$, δm_{100}, M_{Ni}, and M_{ej}. Since the publication of P16 more usable data has become available, partially from public data accessed through the Open supernova Catalog[6] (OSC; Guillochon et al. 2017) and partially from recently published observations; SNe Ic-6 2006dn, IIb SN 2008aq (Modjaz et al. 2014; Bianco et al. 2014; Stritzinger et al. 2018a), Ic-4 SN 2016coi (Prentice et al. 2018a), and GRB-SN 2016jca (Ashall et al. 2017). These new SNe, analysed using the methods described in P16, provide an extension to that database and bring the total sample size to 106.[7] Distributions are constructed using the available objects and the mean and median calculated. The standard deviation of each distribution is calculated and quoted with the mean, this represents the overall scatter of the objects. Using the median, a 1 sigma region is calculated which includes

---

[6]https://sne.space/

[7]Not all of these have sufficient data coverage to be included in every distribution and GRB-SN 2011kl has been excluded as it was magnetar-powered (Greiner et al. 2015).
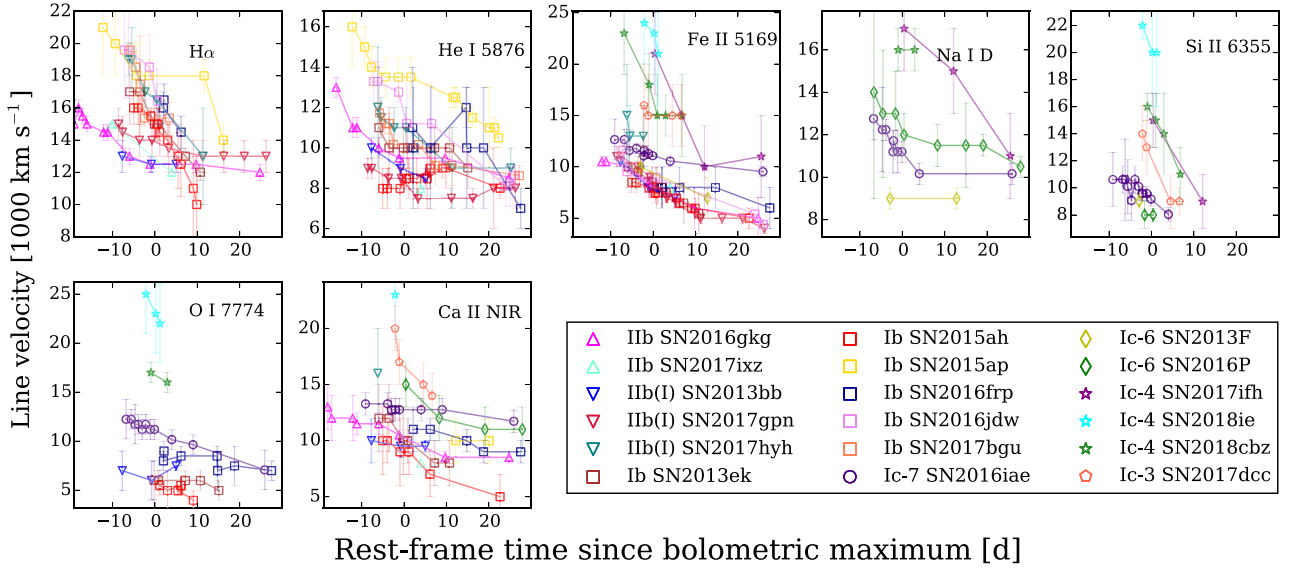
**Figure 7.** The photospheric phase velocity curves of common lines in SE–SNe.
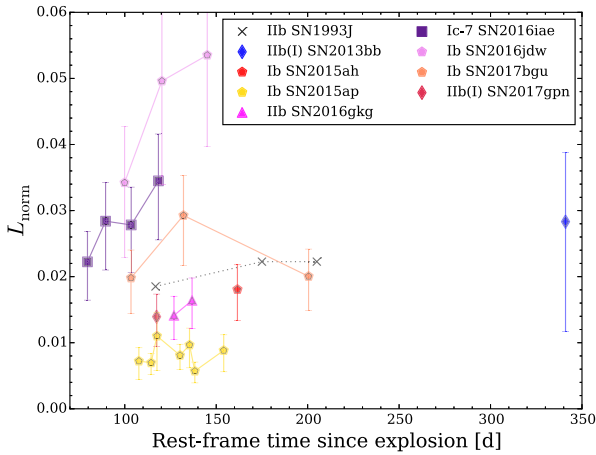
Figure 8. The normalized luminosity of the [O I] $\lambda\lambda$ 6300,6363 line as derived from the nebular and near nebular spectra. Shown for reference is L_{norm} of type IIb SN 1993J (Barbon et al. 1995; Richmond et al. 1996).

34 per cent of the SNe above and below the median, thus enclosing 68 per cent of the objects.

5.1 Distributions of bolometric peak luminosity

The distributions of $\log(L_p)$ are shown by type in Fig. 9, with the statistics in Table 4, where it can be seen that most of the SNe fall within one sigma of their respective medians as expected. The exception to this is SN 2018ie, which is underluminous compared with other SNe Ic-3/4. This cannot be attributed to underestimates in the distance or reddening. As with previous results (Drout et al. 2011; Taddia et al. 2015; Lyman et al. 2016; Prentice et al. 2016; Taddia et al. 2018b) H-rich SNe are the least luminous on average, followed by H-poor/He-rich SNe, narrow lined SNe Ic, and broad lined SNe Ic. GRB-SNe are the most luminous SE–SNe.
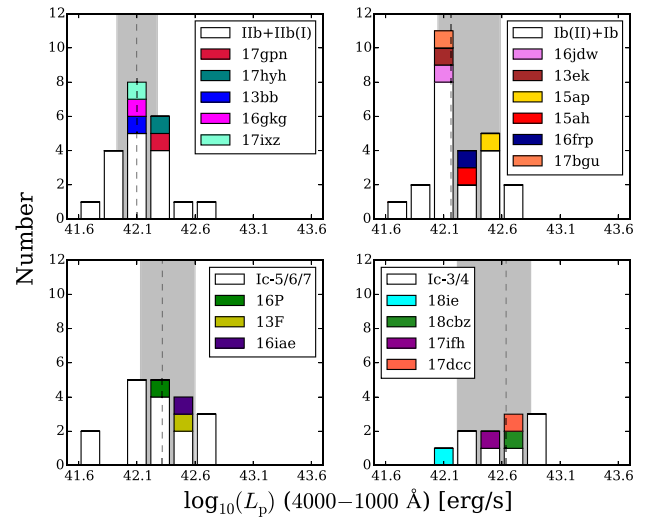
Figure 9. The distributions of $\log(L_p)$ with the new SNe in context, calculated from the 4000–10000 Å bolometric light curves, for SNe grouped by type. Only SNe with an estimated $E(B-V)_{\mathrm{host}}$ are included. The dotted line denotes the median of each distribution while 1σ around the median (enclosing 68 per cent of the objects in the distribution, 34 per cent either side of the median) is given by the grey regions. The distribution in white is SNe from the P16 sample. GRB-SNe are not included.

Table 4. $\log(L_p)$ statistics.

Type	Median [erg s^{-1}]	Mean [erg s^{-1}]	N
IIb + IIb(I)	42.09 ± 0.17	42.13 ± 0.2	21
Ib + Ib(II)	$42.2^{0.4}_{0.1}$	42.3 ± 0.2	25
Ic-5/6/7	$42.3^{0.3}_{0.2}$	42.3 ± 0.3	19
Ic-3/4	$42.6^{0.2}_{0.4}$	42.6 ± 0.3	11
XRF-SNe	42.5 ± 0.2	42.5 ± 0.2	2
GRB-SNe	$42.96^{0.10}_{0.12}$	42.9 ± 0.1	7
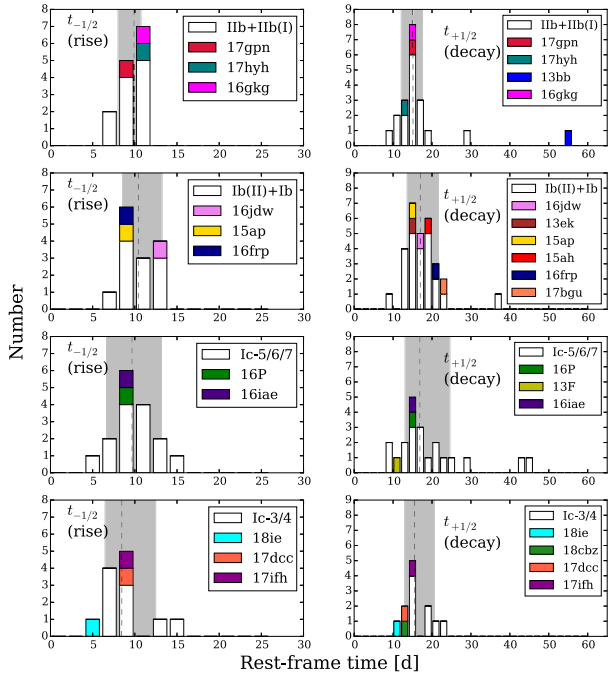
Figure 10. Distributions of $t_{-1/2}$ (left) and $t_{+1/2}$ (right) for the various SN subtypes. SN IIb(I) 2013bb is a clear outlier with $t_{+1/2} \sim 56$ d. The dashed line and grey regions are as in Fig. 9.

Table 5. $t_{-1/2}$ and $t_{+1/2}$ statistics per SN type.

Type	Median [d]	Mean [d]	N
	$t_{-1/2}$		
IIb + IIb(I)	$9.9\pm_{1.9}^{0.8}$	10 ± 1	14
Ib + Ib(II)	$10.4\pm_{1.7}^{2.8}$	11 ± 2	14
Ic-5/6/7	$9.8\pm_{3.1}^{3.3}$	10 ± 2	16
Ic-3/4	$8.6\pm_{2.0}^{3.8}$	9 ± 2	11
XRF-SN	~ 7	~ 7	1
GRB-SNe	$9.7\pm_{1.8}^{1.9}$	10 ± 1	4
	$t_{+1/2}$		
IIb + IIb(I)	$15.1\pm_{3.0}^{2.5}$	17 ± 10	20
Ib + Ib(II)	$17.0\pm_{3.4}^{4.7}$	18 ± 5	29
Ic-5/6/7	$17.5\pm_{4.5}^{7.1}$	20 ± 9	21
Ic-3/4	$15.5\pm_{2.6}^{5.1}$	16 ± 4	11
XRF-SNe	12 ± 2	12 ± 2	2
GRB-SNe	$14.3\pm_{1.9}^{2.7}$	15 ± 2	5

5.2 The distributions of $t_{-1/2}$ and $t_{+1/2}$

The distributions for $t_{-1/2}$ and $t_{+1/2}$ are shown in Fig. 10 and the statistics in Table 5. SN 2013bb is clearly an interesting object with $t_{+1/2} \sim 56$ days, considerably longer than any other supernova in the sample. the decay time of SN 2013F is short but highly uncertain due to lack of photometry.

The distribution of $t_{+1/2}$ is similar to that previously found but, compared with the smaller sample of P16, the differences in $t_{-1/2}$ found in that study between broad lined and non-broad lined SNe has largely vanished. The medians and means for these types in the present sample are within 0.6 d of each other. The Ic broad-line group retains its short average rise time, however there are some long-rise SNe in this group.
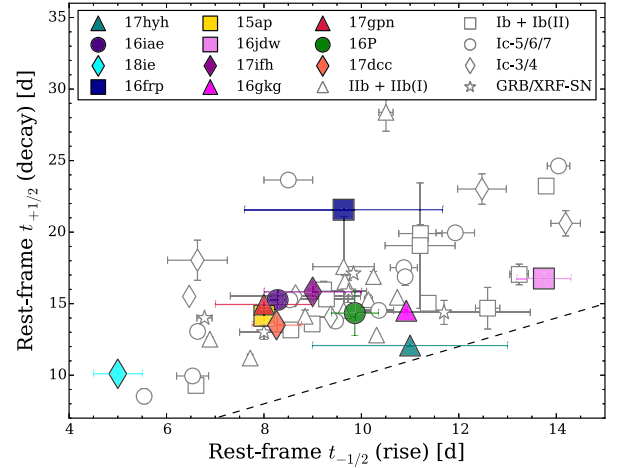
Figure 11. $t_{-1/2}$ against $t_{+1/2}$ for all SE–SN types. The markers denote the SN type, the dashed line is the line of equality, and the white symbols are the P16 sample.

5.2.1 Comparison of $t_{-1/2}$ and $t_{+1/2}$

Fig. 11 shows $t_{+1/2}$ as a function of $t_{-1/2}$. This plot is a measure of diffusion time and is affected by M_{ej}, E_k, power source, and power source distribution. If the SN light curves are powered by different sources (e.g. ^{56}Ni decay, interaction with the circumstellar medium or magnetar spin-down) then presenting the data in this way may reveal different sub-groups, (as attempted by, e.g. Nicholl et al. (2015) for superluminous SNe). For example, the early light curves of SNe IIP are not determined by radioactive heating (see Bersten, Benvenuto & Hamuy 2011), so with $t_{-1/2}$ of a few days but $t_{+1/2}$ of many tens they would be placed in the far upper left of the plot. Likewise, rapidly evolving events (e.g. Drout et al. 2014; Pursiainen et al. 2018; Prentice et al. 2018b) would be found in the extreme lower left hand corner. The SE-SNe are clustered along a similar axis, which suggests that most have the same power source, in this case ^{56}Ni decay. The outliers are the most interesting, as these could represent physical differences. SN 2018ie has both a fast rise and decline (with $t_p < 9$ d) and a low luminosity, all of which the ^{56}Ni-powered Arnett (1982) model struggles to replicate. Such an investigation is outside the scope of this work however.

5.3 The linear decay rate at 100 days

Fig. 12 (top) shows the distribution of δm_{100}, and it can be seen that SN 2013bb is one of the slowest declining SNe. By contrast, SN 2017hyh declines rapidly at ~ 0.029 mag d^{-1}. Most SNe decline faster, with the mean being ~ 0.017 mag d^{-1} regardless of SN type.

Fig. 13 shows δm_{100} as a function of $t_{-1/2}$ and $t_{+1/2}$, both of which are converted to units of mag d^{-1}. As when comparing $t_{-1/2}$ against $t_{+1/2}$, both show a correlation in that a longer time-scale at early times corresponds to a longer time-scale at later times. This is strongest for SNe Ib and SNe Ic-6/7 when considering δm_{100} against $t_{+1/2}$. In the bottom panel it can be seen that SN 2017hyh declines quickly by both metrics but its δm_{100} is the clearest outlier.

Finally, host–galaxy flux contaminates the SN flux at late times, when the SN is less luminous. This could have an impact on the values found here. However, we have one object with templates that allowed a host-subtracted bolometric light curve, SN 2013bb, and find that the host-subtracted δm_{100} increases over the non-subtracted version by just 0.001 mag d^{-1}. However, this effect may be more
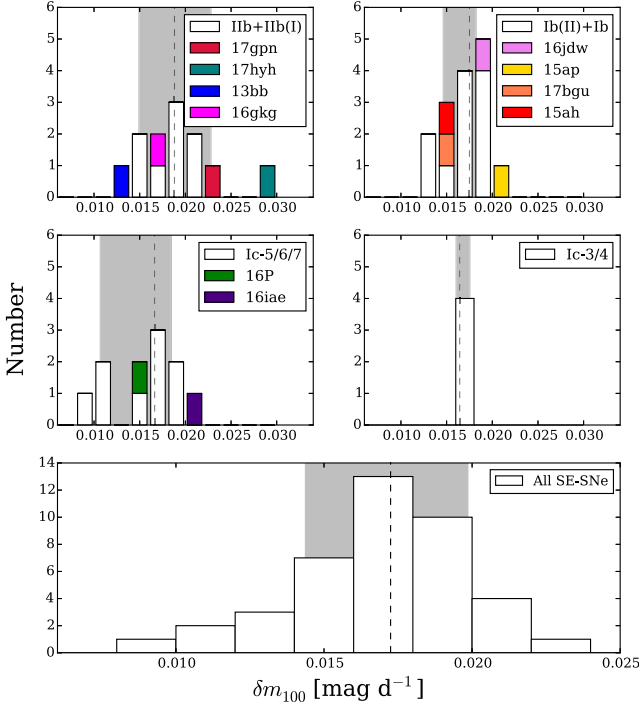
Figure 12. (top) The distribution of late time decay rates for SE–SNe; the median is ∼0.017 mag d^{-1} for all SN types. Only SN 2013bb has had host–galaxy flux subtracted, but the effect of this on δm_{100} was found to be negligible at this phase, ∼0.001 mag d^{-1}. The dashed line and grey regions are as in Fig. 9.
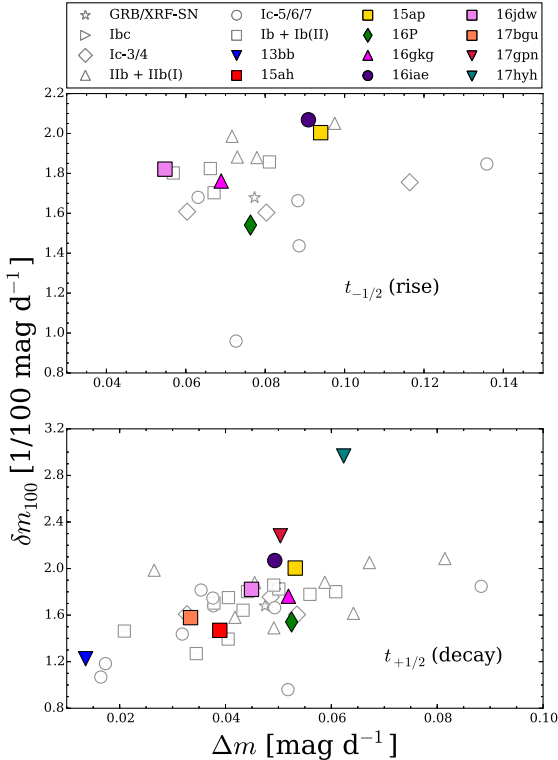
Figure 13. (Top) δm_{100} as a function of $t_{-1/2}$ in units of mag d^{-1}. (Bottom) δm_{100} as a function of $t_{+1/2}$ in units of mag d^{-1}.
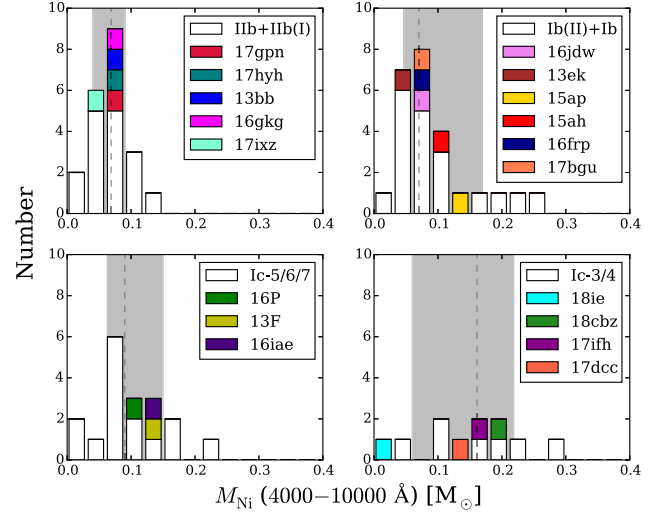
Figure 14. The distribution of $M_{\rm Ni}$ synthesized through explosive Si burning after core-collapse and calculated using the 4000–10 000 Å light curve. Only SNe where $E(B-V)_{\rm host}$ is known are included. The dashed line and grey regions are as in Fig. 9. SNe Ibc have not been classified conclusively as either SNe Ic or SNe Ib.

Table 6. $M_{\rm Ni}$ statistics derived from 4000–10 000 Å light curves.

Type	Median [M$_\odot$]	Mean [M$_\odot$]	N
IIb + IIb(I)	$0.07_{-0.03}^{+0.02}$	0.07 ± 0.03	21
Ib + Ib(II)	$0.07_{-0.02}^{+0.10}$	0.09 ± 0.06	25
Ic-5/6/7	$0.09_{-0.03}^{+0.06}$	0.11 ± 0.09	19
Ic-3/4	$0.16_{-0.10}^{+0.06}$	0.15 ± 0.07	11
XRF-SNe	0.11 ± 0.03	0.11 ± 0.03	2
GRB-SNe	$0.30_{-0.06}^{+0.20}$	0.3 ± 0.1	5

pronounced for brighter hosts, dimmer SNe, or SNe positioned over bright H II regions, where conamination is more prevalent.

6 ^{56}NI AND EJECTA MASSES

Analysis of the bolometric light curves allows for two masses to be calculated; $M_{\rm Ni}$ and $M_{\rm ej}$. The ^{56}Ni mass was calculated for a large sample of SNe in P16; here we add the calculations of the 18 SNe included here plus the 4 new literature SNe. The ejecta mass is calculated for as many of the SNe in P16 as possible, using the line velocities from Prentice & Mazzali (2017), plus the new literature SNe, using the same method as described in Section 3.2.3. A table of ejecta masses can be found in the supplementary material. Here, we consider the respective distributions for different subtypes.

6.1 $M_{\rm Ni}$ distribution

Fig. 14 shows the distribution of $M_{\rm Ni}$ as derived from the 4000 − 10 000 Å light curves for the different SN subtypes. The statistics for these distributions are listed in Table 6.

Our 18 SE–SNe are not unusual in respect of their $M_{\rm Ni}$. The medians of distributions reflect the fact that energetic SNe synthesize the most ^{56}Ni, and He-rich SNe the least. Of the He-rich SNe, both H-rich and H-poor synthesize similar amounts of ^{56}Ni if one considers the median. If one considers the mean then the He-poor explosions

Table 7. M_{ej} statistics in comparison with other work.

Type[†]	Median [M$_\odot$]	Mean [M$_\odot$]	N
	This work		
IIb + IIb(I)	$2.5^{+1.3}_{-0.7}$	2.7 ± 1.0	20
Ib(II) + Ib	$2.0^{+1.2}_{-0.9}$	2.2 ± 0.9	25
Ic-6 + Ic-7	$2.2^{+3.1}_{-0.9}$	3.2 ± 2.4	18
Ic-3 + Ic-4	$3.0^{+0.8}_{-0.7}$	3.0 ± 0.7	12
XRF-SNe	2.8 ± 0.6	2.8 ± 0.6	2
GRB-SNe	$4.3^{+2.5}_{-1.2}$	4.7 ± 1.5	3
All	$2.4^{+1.5}_{-1.0}$	2.8 ± 1.5	80
	Drout et al. (2011)		
Ib	-	$2.0^{+1.1}_{-0.8}$	8
Ic	–	$1.7^{+1.4}_{-0.9}$	11
Ic-BL	-	$4.7^{+2.3}_{-1.8}$	4
'Engine-driven SNe'	–	$3.6^{+2.0}_{-1.6}$	3
	Taddia et al. (2015)		
Ib	–	3.6 ± 0.6	6
Ic	–	5.75 ± 2.09	3
Ic-BL	–	5.39 ± 1.30	4
	Lyman et al. (2016)		
IIb	-	2.2 ± 0.8	9
Ib	-	2.6 ± 1.1	13
Ic	-	3.0 ± 2.8	8
Ic-BL	-	2.9 ± 2.2	9
	Taddia et al. (2018b)		
IIb	–	4.3 ± 2.0	10
Ib	–	3.8 ± 2.1	10
Ic	–	2.1 ± 1.0	11

Notes. [†] See Section 1 for how the classification schemes relate.

result in more ^{56}Ni, which is in line with previous studies. Fig. 14 shows that the M_{Ni} of the SNe Ib is more skewed than that of the H-rich SNe which is where the discrepancy in these two measurements lies. Consequently, we can say (for the most part) that the He-rich SNe produce similar masses of ^{56}Ni but there exists a tail of higher M_{Ni} in the H-poor distribution.

6.2 Ejecta masses

Analysis of ejecta mass for SE–SNe has also been done previously, but for smaller samples (see Drout et al. 2011; Taddia et al. 2015; Lyman et al. 2016; Taddia et al. 2018b). With the exception of Taddia et al. (2018b), where a hydrodynamics code was used, the procedure for determining M_{ej} was similar to that used here, i.e. the method of Arnett (1982). In most cases, an opacity parameter κ of 0.05–0.07 g cm^{-2} was used, although Drout et al. (2011) assumed a typical value for v_{ph} rather than using measurements, and t_p is often similar, but not identical, to that used here. These variations in input parameters can go some way to explaining differences in the results (see Table 7). Additionally, differences between M_{ej} calculated from photospheric phase spectral modelling and light curve modelling may arise for some SNe with long rise times and broad lines. For example, M_{ej} of SN 1998bw differs between spectral modelling (10 M$_\odot$; Mazzali et al. 2013) and light curve fitting ($\sim$5 M$_\odot$; e.g. this work, Lyman et al. 2016). The ejected mass is better constrained from nebular models however (e.g. Mazzali et al. 2001, 2007, 2010).

Table 3 gives M_{ej} for the SNe investigated here. Fig. 15 shows the
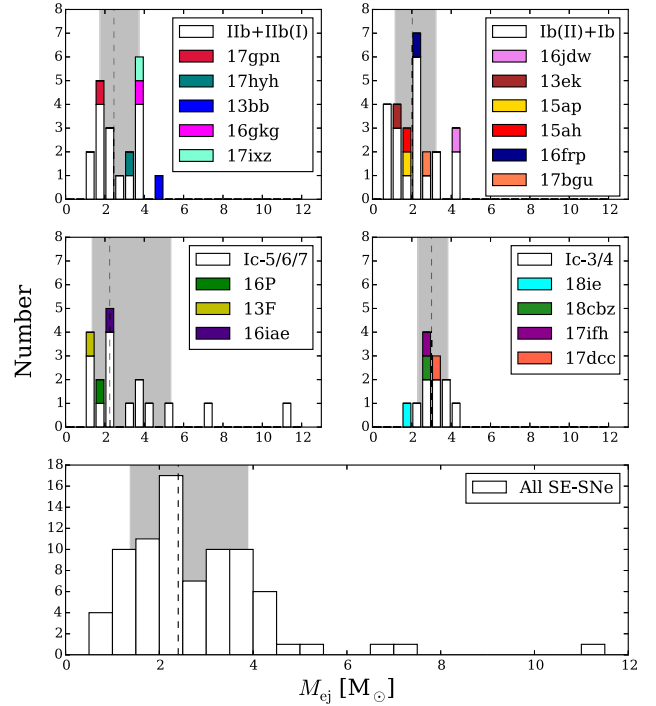
Figure 15. The M_{ej} distribution of SNe IIb + IIb(I) (top left), SNe Ib(II) and Ib (top right), SNe Ic-5/6/7 (middle left), and SNe Ic-3/4 (middle right), and all SE-SNe including GRB and XRF-SNe (lower panel). The dashed line and grey regions are as in Fig. 9.

distribution of M_{ej} for each subtype. Our 18 SNe are, for the most part, typical in M_{ej} but there are two clear exceptions. SN 2013bb is the highest mass H-rich SN in the sample with $M_{ej} \sim 4.8$ M$_\odot$. This makes sense in the context of its broad light curve and slow spectroscopic evolution. Type Ib SN 2016jdw has $M_{ej} \sim 4.3$ M$_\odot$, and the only equivalent SNe Ib are SN 2009jf and the peculiar SN 2007uy with $M_{ej} \sim 4.2$ M$_\odot$.

Most of the distributions are unimodal, with the exception of that for the H-rich SNe where there are two peaks around 1.9 and 3.9 M$_\odot$ which appears to coincide with more compact and extended progenitors respectively (as determined by the luminosity and duration of the shock cooling tail). The distribution of SNe Ic-6/7 ejecta masses shows a large range of possible values which hints at a wide range of progenitor masses. The results here show that the median M_{ej} is $<$5 M$_\odot$ for all SNe. The bulk distribution for all SE-SNe has $<M_{ej}>=2.8 \pm 1.5$ M$_\odot$ (median M_{ej}=2.4 M$_\odot$) and shows no clear indication of bimodality, but does have a 'high mass' tail.

7 DISCUSSION

7.1 Average M_{ej} and lack of bimodality

The overlap in the M_{ej} distributions for different SN sub-types suggests that the progenitors of many of these SNe may be similar. If one assumes a 1.4 M$_\odot$ neutron star (NS) remnant[8] then $M_{ej} + M_{NS} = M_{COcore} < 5$ M$_\odot$ for the vast majority of SE-SNe. Given that there are two possible progenitor pathways, one from low-mass stars

---

[8]Assuming SNe do not occur when the core collapses directly to a black hole.

stripped through binary interaction and one from high-mass single stars, it may be expected that there would be two M_{ej} distributions present.

The distribution of all SNe and for the SNe Ic appears unimodal. However, it was previously mentioned that M_{ej} of GRB-SNe could be underestimated with this method and that spectral modelling has shown these SNe to have $M_{ej} \sim 10\,M_\odot$ (Mazzali et al. 2003, 2013; Ashall et al. 2017). In this case, a bimodality would appear with a second peak around $10\,M_\odot$, and it may point to GRB-SNe resulting from a different population to other SE-SNe. However, as these occur in low-metallicity environments (Modjaz et al. 2008; Japelj et al. 2016; Vergani et al. 2017; Japelj et al. 2018) their progenitors may still have had significant binary interaction in order to lose their H and He envelopes.

The lack of bimodality present in the distributions could result from preference for one evolutionary pathway over the other. That the mean ejecta mass is low and the number of SE-SNe so high compared to the rate of WR stars (Smith et al. 2011) suggests that stripping of stars $<30\,M_\odot$ through binary interaction is the dominant pathway. This can be partly reconciled if one considers variations in the IMF that allow the formation of more high-mass stars (e.g. Schneider et al. 2018).

7.2 Linking ejecta mass to initial mass

The ejecta masses for He-rich SNe, and L_{norm} curves from nebular spectra, are consistent with the final masses of stars with M_{ZAMS} of 10–18 $M_\odot$ stripped in binary environments (Yoon, Dessart & Clocchiatti 2017; Limongi 2017). This may also be similarly true for SNe Ic, because the difficulty in the single star scenario is in explaining the low mean ejecta mass of SNe Ic, with the condition that the mass of He in the pre-explosion envelope $M_{He} < 0.14\,M_\odot$ (Hachinger et al. 2012), and with the relative observed rates of SNe Ic.

The models of Woosley, Langer & Weaver (1993) showed it was possible to obtain a pre-SN mass star of $\sim 4\,M_\odot$ from a $60\,M_\odot$ star and for it to be below the M_{He} limit. Chieffi & Limongi (2013) find progenitors compatible with our criteria from rotating single stars with $M_{ZAMS} = 20$–$25\,M_\odot$. These are He-free and have $M_{ej} \leq 5\,M_\odot$ assuming a NS remnant. Stars with M_{ZAMS} greater than this have compatible M_{ej}, towards the tail of the M_{ej} distribution.

Yoon (2017) adapted the mass-loss rates of Wolf-Rayet stars and better matched the observed properties (low ejecta masses) of SNe Ic, obtaining pre-SNe stars of $\sim 5\,M_\odot$ from He stars of initial mass $M = 10$–$12\,M_\odot$ that could explode as SNe Ic with the ejecta masses we find here. Yoon (2017) state that their $15\,M_\odot$ He stars arise from stars with $M_{ZAMS} = 30$–$40\,M_\odot$, thus the 10–12 $M_\odot$ He stars would be expected to have M_{ZAMS} below this.

None of the models from Georgy et al. (2009) fulfilled both the M_{ej} and M_{He} criteria, regardless of metallicity. At explosion, they were too massive and too rich in elements heavier than oxygen. The $M_{ZAMS} = 32$–$40\,M_\odot$ models of Georgy et al. (2012) that include rotation fare better, as these are within the upper bounds of the He-poor M_{ej} distributions ($M_{em} \geq 7\,M_\odot$) and fulfil the M_{He} criteria. McClelland & Eldridge (2016) find viable SN Ic progenitors from a stripped $30\,M_\odot$ star, again at the high end of our M_{ej} distribution, with $M_{em} \geq 5.5\,M_\odot$ for different metallicities. Groh et al. (2013) find models that fit the M_{He} criteria from $M_{ZAMS} > 32\,M_\odot$ rotating stars but which predict pre-SN masses of $M > 10\,M_\odot$. Even accounting for large uncertainties in determining the ejecta mass, most of the values calculated here would have to increase by a factor of 4 to match the resulting C/O core mass ($\sim 10\,M_\odot$) of a

star with $M_{ZAMS} = 30\,M_\odot$. Thus, these results suggest that SE-SNe, even SNe Ic, predominantly occur from $<30\,M_{ZAMS}$ stars stripped by binary interaction. That is not to say they arise from the same type of stars however, the work of Modjaz et al. (2011) investigated metallicities at SN explosion sites and showed that SNe Ib and SNe Ic almost certainly arise from different populations (but see Kuncarayakti et al. 2018).

7.3 Broader implications

These SNe and their progenitors can have several significant impacts:

(i) The overlap in SNe II and SN Ib/c progenitor masses supports the view that more massive stars may not explode (though there are windows of explodability; O'Connor & Ott 2011; Sukhbold & Woosley 2014; Sukhbold, Woosley & Heger 2018) and instead collapse directly into black holes. If so, this would result in the loss of some fraction of their elemental yields.

(ii) Low mass binary progenitors resulting in SNe Ib/c can lead to the formation of NS binaries. The binary system is required to be close in order to strip the more massive star, leading to a larger gravitational potential, which in turn reduces the probability of the system becoming unbound when the stars explode. Consequently, SE–SNe systems may contribute to the sources of short GRBs and kilonovae (see Tauris et al. 2013; Tauris, Langer & Podsiadlowski 2015; Moriya et al. 2017, in relation to ultra-stripped SNe).

(iii) The results of the previous section suggest that high metallicity is not required to strip the star of its outer envelope (via line-driven winds) because interaction with a companion can do so. Consequently, these events could occur earlier in the history of the Universe.

(iv) The progenitors of SE–SNe are in the theoretical mass regime of SNe II, meaning that these stars would explode regardless. That they tend to have higher E_k than other SNe means that the dynamical impact of CC–SNe on the local environment in the early Universe may be underestimated.

(v) The pre-explosion star will be highly stripped and hot, either a WR star or a He star. These stars emit copious amounts of UV radiation (e.g. Götberg et al. 2018) which can ionize the surrounding ISM.

(vi) For an observed fractional rate of events, the O yield per SE–SN is lower for the binary pathway (low mass progenitors) than for single stars (high mass progenitors). If the majority of SE–SNe progenitors are low mass stars, the overall O yield per CC–SN decreases.

8 CONCLUSIONS

This work has presented observations and analysis of 18 SE-SNe discovered between 2013 and 2018. These data have been mostly collected on behalf of (e)PESSTO, a Liverpool Telescope observing campaign focused on SE-SNe, and the LCO Supernova Key Project. The sample consists of 5 H/He-rich SNe, 6 H-poor/He-rich SNe, 3 SNe Ic-6/7 and 4 SNe Ic-3/4.

Most of the events observed in this work could be described as typical; their properties fall within the broader distributions of their subtype. There are, however, some key extremes. The type IIb(I) SN 2013bb has a broad light curve, and its ejecta mass of $\sim 4.8\,M_\odot$ makes it the most massive H/He-rich SNe yet found. Another SN of this type, SN 2017hyh, has the highest velocity lines of any H-rich SE–SNe discovered so far with $v_{H\alpha} \sim 17\,000\,\mathrm{km\,s^{-1}}$ at

maximum light. This SN also has an extremely rapid late decay rate at $\delta m_{100} = 0.029$ mag d^{-1}. SN Ib 2016jdw has a broad light curve and also line velocities that are amongst the highest for SNe of this type. With $M_{ej} \sim 4.3$ M$_\odot$, it is significantly outside the typical SN Ib ejecta mass distribution and is only matched by the SN 1999ex and peculiar Ib SN 2007uy. The Ic-4 SN 2018ie has a short rise time ($t_p \sim 8$ d), high velocity lines ($> 20\,000$ km s^{-1}) and is the least luminous SNe of this type known.

The M_{ej} mass distribution of H-rich SNe is bimodal with two peaks around 1.9 and 3.9 M$_\odot$. The SNe associated with these peaks are typically those without/with a shock cooling tail respectively. This is associated with compact/extended progenitor envelopes. The SN Ic-6/7 distribution has a low mass (~ 2.2 M$_\odot$) peak but a high mass tail, suggesting a large range of pre-explosion stellar masses. A full ejecta mass distribution of 80 SE-SNe appears unimodal with median $M_{ej} = 2.4 \pm^{1.5}_{1.0}$ M$_\odot$ and a mean ejecta mass of 2.8 ± 1.5 M$_\odot$. Adding a 1.4 M$_\odot$ NS remnant to M_{ej} gives a total pre-explosion core mass of < 5 M$_\odot$ for the vast majority of SE-SNe.

Eight SNe had nebular phase spectra, using M_{Ni}, $L_{[OI]}$, and the methods of Jerkstrand et al. (2015) it was found that all these objects, with the exception of SN 2016jdw, were compatible with model progenitors of $M_{ZAMS} < 17$ M$_\odot$. The progenitor of SN 2016jdw was unlikely to have been much more massive than this. Comparison of M_{ej} with stellar evolution models leads to the conclusion that the vast majority of SE-SN progenitor stars have $M_{ZAMS} < 30$ M$_\odot$, and are stripped by binary interaction. In this case, the mass and metallicity dependence on envelope stripping is reduced and suggests that these kinds of events could have occurred in the early universe. Stripped stars are copious emitters of UV radiation and will ionize their local surroundings.

These results further the tension between progenitor masses derived from light curve fitting and spectral modelling, single star stellar evolution models, and examination of explosion environments. The theoretical ($M_{ZAMS} = 12$–25 M$_\odot$) and observational ($M_{ZAMS} = 7$–18 M$_\odot$) range of SN II progenitors overlaps with that found in this and previous studies, yet it is clear that the explosion environments are different (SNe Ib/c tend to be found in or closer to H II regions). As has been noted, the latter suggest massive progenitors > 30 M$_\odot$ for many SE-SNe which appear to have low ejecta mass. This discrepancy remains unsolved and should be a focus of future investigation. A way to reconcile or identify problems, moving away from simple 1D analytical light curve models, would be to use spectral modelling in order to investigate the abundance tomography of the SN ejecta (e.g. the elemental abundance as a function of mass and velocity) then link this back to theoretical models of pre-explosion massive stars. Fortunately, we are now entering a time where the increase in number of well sampled SE-SN means the required parameter space can be mapped.

REFERENCES

Aldering G., Humphreys R. M., Richmond M., 1994, AJ, 107, 662
Anderson J. P., Habergham S. M., James P. A., Hamuy M., 2012, MNRAS, 424, 1372
Arcavi I. et al., 2011, ApJ, 742, L18
Arcavi I. et al., 2017, ApJ, 837, L2
Arnett W. D., 1982, ApJ, 253, 785
Ashall C. et al., 2017 preprint (arXiv:1702.04339)
Ashall C., Mazzali P., Bersier D., Hachinger S., Phillips M., Percival S., James P., Maguire K., 2014, MNRAS, 445, 4427
Barbon R., Benetti S., Cappellaro E., Patat F., Turatto M., Iijima T., 1995, A&AS, 110, 513
Barnsley R. M., Smith R. J., Steele I. A., 2012, Astron. Nach., 333, 101
Bersten M. C. et al., 2014, AJ, 148, 68
Bersten M. C. et al., 2018, Nature, 554, 497
Bersten M. C., Benvenuto O., Hamuy M., 2011, ApJ, 729, 61
Bianco F. B. et al., 2014, ApJS, 213, 19
Brown T. M. et al., 2013, PASP, 125, 1031
Bundy K. et al., 2015, ApJ, 798, 7
Cao Y. et al., 2013, ApJ, 775, L7
Cardelli J. A., Clayton G. C., Mathis J. S., 1989, ApJ, 345, 245
Chieffi A., Limongi M., 2013, ApJ, 764, 21
Childress M. J. et al., 2016, PASA, 33, e055
Chornock R. et al., 2011, ApJ, 739, 41
Crockett R. M. et al., 2008, MNRAS, 391, L5
Crowther P. A., 2007, ARA&A, 45, 177
Crowther P. A., 2013, MNRAS, 428, 1927
Crowther P. A., Drissen L., Abbott J. B., Royer P., Smartt S. J., 2003, A&A, 404, 483
Drout M. R. et al., 2011, ApJ, 741, 97
Drout M. R. et al., 2014, ApJ, 794, 23
Eisenstein D. J. et al., 2011, AJ, 142, 72
Eldridge J. J., Maund J. R., 2016, MNRAS, 461, L117
Eldridge J. J., Fraser M., Smartt S. J., Maund J. R., Crockett R. M., 2013, MNRAS, 436, 774
Faber S. M. et al., 2003, in Iye M., Moorwood A. F. M., eds, Proc. SPIE Vol. 4841, Instrument Design and Performance for Optical/Infrared Ground-based Telescopes. p. 1657
Filippenko A. V. et al., 1995, ApJ, 450, L11
Folatelli G. et al., 2014, ApJ, 792, 7

Folatelli G., Bersten M. C., Kuncarayakti H., Benvenuto O. G., Maeda K., Nomoto K., 2015, ApJ, 811, 147

Fox O. D. et al., 2014, ApJ, 790, 17

Fremling C. et al., 2014, A&A, 565, A114

Fremling C. et al., 2018, A&A, 618, A37

Fukugita M., Ichikawa T., Gunn J. E., Doi M., Shimasaku K., Schneider D. P., 1996, AJ, 111, 1748

Gal-Yam A., Mazzali P. A., Manulis I., Bishop D., 2013, PASP, 125, 749

Galbany L. et al., 2014, A&A, 572, A38

Galbany L. et al., 2016, A&A, 591, A48

Galbany L. et al., 2018, ApJ, 855, 107

Georgy C., Meynet G., Walder R., Folini D., Maeder A., 2009, A&A, 502, 611

Georgy C., Ekström S., Meynet G., Massey P., Levesque E. M., Hirschi R., Eggenberger P., Maeder A., 2012, A&A, 542, A29

Götberg Y., de Mink S. E., Groh J. H., Kupfer T., Crowther P. A., Zapartas E., Renzo M., 2018, A&A, 615, A78

Greiner J. et al., 2008, PASP, 120, 405

Greiner J. et al., 2015, Nature, 523, 189

Groh J. H., Meynet G., Georgy C., Ekström S., 2013, A&A, 558, A131

Guillochon J., Parrent J., Kelley L. Z., Margutti R., 2017, ApJ, 835, 64

Hachinger S., Mazzali P. A., Taubenberger S., Hillebrandt W., Nomoto K., Sauer D. N., 2012, MNRAS, 422, 70

Iwamoto K. et al., 1998, Nature, 395, 672

Japelj J. et al., 2016, A&A, 590, A129

Japelj J., Vergani S. D., Salvaterra R., Renzo M., Zapartas E., de Mink S. E., Kaper L., Zibetti S., 2018, A&A, 617, A105

Jerkstrand A., Smartt S. J., Fraser M., Fransson C., Sollerman J., Taddia F., Kotak R., 2014, MNRAS, 439, 3694

Jerkstrand A., Ergon M., Smartt S. J., Fransson C., Sollerman J., Taubenberger S., Bersten M., Spyromilio J., 2015, A&A, 573, A12

Jones D. O., Dimitriadis G., Pan Y. C., Foley R. J., 2017, Transient Name Server Classification Report, 1464

Kilpatrick C. D. et al., 2017, MNRAS, 465, 4650

Krühler T. et al., 2008, ApJ, 685, 376

Kumar B. et al., 2013, MNRAS, 431, 308

Kuncarayakti H. et al., 2018, A&A, 613, A35

Limongi M., 2017, Supernovae from Massive Stars. p. 513

Lin H., Xiang D., Rui L., Wang X., Wang J., Qiu P., Zhang T., Zhang J., 2018, Transient Name Server Classification Report, 94

Liu Y.-Q., Modjaz M., Bianco F. B., Graur O., 2016, ApJ, 827, 90

Lyman J. D., Bersier D., James P. A., Mazzali P. A., Eldridge J. J., Fraser M., Pian E., 2016, MNRAS, 457, 328

Maeda K. et al., 2008, Science, 319, 1220

Marino R. A. et al., 2013, A&A, 559, A114

Matheson T., Filippenko A. V., Li W., Leonard D. C., Shields J. C., 2001, AJ, 121, 1648

Mauerhan J. C. et al., 2015, MNRAS, 453, 4467

Maund J. R. et al., 2011, ApJ, 739, L37

Maund J. R. et al., 2015, MNRAS, 454, 2580

Maund J. R., 2018, MNRAS, 476, 2629

Maund J. R., Smartt S. J., Kudritzki R. P., Podsiadlowski P., Gilmore G. F., 2004, Nature, 427, 129

Maund J. R., Pastorello A., Mattila S., Itagaki K., Boles T., 2016, ApJ, 833, 128

Mazzali P. A. et al., 2003, ApJ, 599, L95

Mazzali P. A. et al., 2005, Science, 308, 1284

Mazzali P. A. et al., 2006, ApJ, 645, 1323

Mazzali P. A. et al., 2007, ApJ, 670, 592

Mazzali P. A. et al., 2014, MNRAS, 439, 1959

Mazzali P. A., Nomoto K., Patat F., Maeda K., 2001, ApJ, 559, 1047

Mazzali P. A., Deng J., Hamuy M., Nomoto K., 2009, ApJ, 703, 1624

Mazzali P. A., Maurer I., Valenti S., Kotak R., Hunter D., 2010, MNRAS, 408, 87

Mazzali P. A., Walker E. S., Pian E., Tanaka M., Corsi A., Hattori T., Gal-Yam A., 2013, MNRAS, 432, 2463

McClelland L. A. S., Eldridge J. J., 2016, MNRAS, 459, 1505

Milisavljevic D. et al., 2014, in American Astronomical Society Meeting Abstracts #223. p. 354.29

Modjaz M. et al., 2014, AJ, 147, 99

Modjaz M., Kirshner R. P., Blondin S., Challis P., Matheson T., 2008, ApJ, 687, L9

Modjaz M., Kewley L., Bloom J. S., Filippenko A. V., Perley D., Silverman J. M., 2011, ApJ, 731, L4

Modjaz M., Liu Y. Q., Bianco F. B., Graur O., 2016, ApJ, 832, 108

Morales-Garoffolo A. et al., 2014, MNRAS, 445, 1647

Moriya T. J. et al., 2017, MNRAS, 466, 2085

Nagy A. P., 2018, ApJ, 862, 143

Nakamura T., Mazzali P. A., Nomoto K., Iwamoto K., 2001, ApJ, 550, 991

Nicholl M. et al., 2015, MNRAS, 452, 3869

Nomoto K., Iwamoto K., Suzuki T., 1995, Phys. Rep., 256, 173

O'Connor E., Ott C. D., 2011, ApJ, 730, 70

Olivares E F. et al., 2015, A&A, 577, 15

Piascik A. S., Steele I. A., Bates S. D., Mottram C. J., Smith R. J., Barnsley R. M., Bolton B., 2014, in Ground-based and Airborne Instrumentation for Astronomy V. p. 91478H

Pignata G. et al., 2009, in Giobbi G., Tornambe A., Raimondo G., Limongi M., Antonelli L. A., Menci N., Brocato E., eds, American Institute of Physics Conference Series Vol. 1111, American Institute of Physics Conference Series. p. 551, preprint (arXiv:0812.4923)

Poznanski D., Ganeshalingam M., Silverman J. M., Filippenko A. V., 2011, MNRAS, 415, L81

Poznanski D., Prochaska J. X., Bloom J. S., 2012, MNRAS, 426, 1465

Prentice S. J. et al., 2016, MNRAS, 458, 2973(P16)

Prentice S. J. et al., 2018a, MNRAS, 478, 4162

Prentice S. J. et al., 2018b, ApJ, 865, L3

Prentice S. J., Mazzali P. A., 2017, MNRAS, 469, 2672

Pursiainen M. et al., 2018, MNRAS, 481, 894

Richmond M. W. et al., 1996, AJ, 111, 327

Richmond M. W., Treffers R. R., Filippenko A. V., Paik Y., Leibundgut B., Schulman E., Cox C. V., 1994, AJ, 107, 1022

Ryder S. D. et al., 2018, ApJ, 856, 83

Sana H. et al., 2012, Science, 337, 444

Schlafly E. F., Finkbeiner D. P., 2011, ApJ, 737, 103

Schneider F. R. N. et al., 2018, Science, 359, 69

Shivvers I. et al., 2017, PASP, 129, 054201

Skrutskie M. F. et al., 2006, AJ, 131, 1163

Smartt S. J. et al., 2015, A&A, 579, A40

Smartt S. J., 2009, ARA&A, 47, 63

Smith N., Li W., Filippenko A. V., Chornock R., 2011, MNRAS, 412, 1522

Steele I. A. et al., 2004, in Oschmann J. M., Jr., ed., Proc. SPIE Vol. 5489, Ground-based Telescopes. p. 679

Stevance H. F. et al., 2016, MNRAS, 461, 2019

Stevance H. F. et al., 2017, MNRAS, 469, 1897

Stritzinger M., Leibundgut B., 2005, A&A, 431, 423

Stritzinger M. D. et al., 2018a, A&A, 609, A134

Stritzinger M. D. et al., 2018b, A&A, 609, A135

Sukhbold T., Woosley S. E., 2014, ApJ, 783, 10

Sukhbold T., Woosley S. E., Heger A., 2018, ApJ, 860, 93

Taddia F. et al., 2015, A&A, 574, A60

Taddia F. et al., 2016, A&A, 592, A89

Taddia F. et al., 2018b, A&A, 609, A136

Taddia F., Sollerman J., Fremling C., Karamehmetoglu E., Barbarino C., Lunnan R., West S., Gal-Yam A., 2019, A&A, 621, A64

Tanaka M. et al., 2009, ApJ, 700, 1680

Tartaglia L. et al., 2017, ApJ, 836, L12

Tartaglia L. et al., 2018, ApJ, 853, 62

Tauris T. M., Langer N., Moriya T. J., Podsiadlowski P., Yoon S.-C., Blinnikov S. I., 2013, ApJ, 778, L23

Tauris T. M., Langer N., Podsiadlowski P., 2015, MNRAS, 451, 2123

Tonry J. L. et al., 2018, PASP, 130, 064505

Valenti S. et al., 2008a, MNRAS, 383, 1485

Valenti S. et al., 2008b, ApJ, 673, L155

Valenti S. et al., 2012, ApJ, 749, L28

Van Dyk S. D. et al., 2014, AJ, 147, 37

Van Dyk S. D. et al., 2018, ApJ, 860, 90

Van Dyk S. D., de Mink S. E., Zapartas E., 2016, ApJ, 818, 75

Vergani S. D. et al., 2017, A&A, 599, A120

Wang L., Wheeler J. C., 2008, ARA&A, 46, 433

Woosley S. E., 1993, ApJ, 405, 273

Woosley S. E., Langer N., Weaver T. A., 1993, ApJ, 411, 823

Yamanaka M. et al., 2017, ApJ, 837, 1

Yaron O., Gal-Yam A., 2012, PASP, 124, 668

Yoon S.-C., 2017, MNRAS, 470, 3970

Yoon S.-C., Dessart L., Clocchiatti A., 2017, ApJ, 840, 10

Zapartas E. et al., 2017, ApJ, 842, 125

Zhang J., Wang X., 2016, The Astronomer's Telegram, 8563

SUPPORTING INFORMATION

Supplementary data are available at *MNRAS* online.

Figre S1: (Top left) The spectra of SN 2016P without host emission line removal. (Top right) Comparison with Ic-4 SNe 2002ap. The lines of SN 2002ap are much broader and at higher velocity. (Lower left) Comparison with SN 1994I, the major features align, although the velocities of SN 1994I are typically higher (except for Na i D). (Lower right) Comparison with Ic-7 SN 2007 gr. The velocities are broadly consistent but there are more features in the spectra SN 2007gr, albeit with a higher S/N

Figure S2: The spectra of SN 2013F, epochs are relative to maximum light.

Figure S3: Spectroscopic observations of SN 2013bb.

Figure S4: Spectroscopic observations of SN 2013ek.

Figure S5: Spectroscopic observations of SN 2015ah.

Figure S6: Spectroscopic observations of SN 2015ap.

Figure S7: Spectroscopic observations of SN 2016P.

Figure S8: Spectroscopic observations of SN 2016frp.

Figure S9: Spectroscopic observations of SN 2016iae.

Figure S10: Spectroscopic observations of SN 2016jdw.

Figure S11: Spectroscopic observations of SN 2017bgu.

Figure S12: Spectroscopic observations of SN 2017dcc.

Figure S13: Spectroscopic observations of SN 2017gpn.

Figure S14: Spectroscopic observations of SN 2017ifh.

Figure S15: Spectroscopic observations of SN 2017ixz.

Figure S16: Spectroscopic observations of SN 2018ie.

Figure S17: Spectroscopic observations of SN 2018cbz.

Table S1: 4000–10000 Å bolometric light curve properties of SNe in the extended P16 sample.

Table S2: Derived $E(B - V)_{host}$ for SNe in P16 and updated parameters

Table S3: Table of δm_{100} values for the extended P16 sample.

Table S4: M_{ej} of the extended P16 sample SNe and comparison with M_{ej} from spectral modelling and hydrodynamics codes.

Please note: Oxford University Press is not responsible for the content or functionality of any supporting materials supplied by the authors. Any queries (other than missing material) should be directed to the corresponding author for the article.

APPENDIX: THE HOST GALAXIES

This section briefly details the host galaxies of some of the SNe, where such analysis could be conducted.

A1 SN 2013F

The host galaxy of SN 2103F is IC 5325, a face-on spiral of type SABbc with a heliocentric recession velocity of 1503 km s^{-1}, giving an adopted distance of 20.9 Mpc and a distance modulus of 31.60 mag. The galaxy has a B-band absolute magnitude $M_{B, 0} = -19.8$, which, when combined with its classification, means that it closely resembles the Milky Way. Given that SN2013F occurred in the inner disk, just 1.9 kpc from the nucleus, the local metallicity was probably slightly higher than solar, although we are not aware of any direct measurements for this galaxy. GALEX imaging indicates strong star formation throughout the central disk of IC 5325.

A2 SN 2013bb

The host galaxy of SN 2013bb, NGC 5504, is a bright face-on spiral of type SAB(s)bc, with a extinction-corrected *B*-band absolute magnitude of –20.91 mag. It has strong spiral structure, and some indications of tidal disturbance, probably due to two close but fainter companions, IC 4383 and UGC 9086, which have identical recession velocities and are only 1.8 and 2.2 arcminutes in projected separation from NGC 5504, respectively. SN 2013bb exploded 10.5 kpc in projected distance from the nucleus of NGC 5504, on the outer edge of a strong spiral arm, and hence in the outer parts of a bright galaxy with a strong similarity to the Milky Way.

A3 Type Ib SN 2013ek

SN 2013ek occurred in NGC 6984, a bright SBc spiral with a recession velocity of 4670 km s^{-1}, giving a corrected Hubble flow distance of 67.5 Mpc and a distance modulus of 34.15 mag. The galaxy has a B-band absolute magnitude $M_{B, 0} = -21.3$ mag, and the SN occurred at a projected galactocentric radius of 3.1 kpc, leading to an inferred metallicity that is likely to be somewhat supersolar. SN 2013ek exploded less than 0.4 arcsec from the type Ic-7 SN 2012im (Milisavljevic et al. 2014).

A4 The type Ib SN 2015ah

The host galaxy of SN 2015ah is a face-on late-type barred spiral, classified in NED as SABcd, with strong spiral structure, although the supernova occurred in a region between the main arms on a short spiral arm spur. The offset from the nucleus of the galaxy corresponds to a projected radial distance of 4.0 kpc, in the central disk regions, which in terms of likely metallicity of the host environment may offset the low luminosity of the galaxy, $M_{B, 0} = -19.29$ mag for our adopted distance. So, even though there are no direct measurements of star formation activity or metallicity at the SN location, it appears likely to have moderate recent star formation, and approximately solar metallicity.

A5 Type Ib SN 2015ap

The host galaxy of SN 2015ap is IC 1776, an SBd late-type barred spiral galaxy with a heliocentric recession velocity of 3410 km s^{-1} ($z = 0.0114$), giving an inferred distance of 45.1 Mpc and a distance modulus of 33.27 mag. The absolute B-band magnitude of the galaxy is $M_{B, 0} = -19.6$ mag, and SN2015ap occurred quite far out in the disk, 7.2 kpc from the nucleus, where the metallicity is likely to be approximately solar. The most striking aspect of the local environment of SN 2015ap is that it lies in an extended
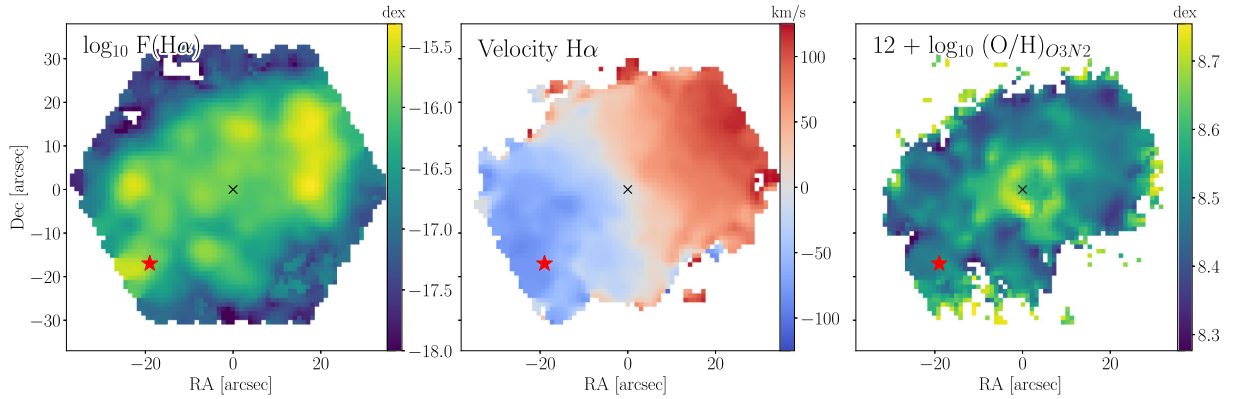
Figure A1. 2MASXJ07470232 + 2646347, the host of SN 2017ixz in Hα flux (left), Hα velocity (centre), and oxygen abundance (right).

complex of extremely vigorous star formation, which is easily the brightest such complex within IC 1776.

A6 SN 2016P

NGC 5374 is a bright, strongly-barred Milky-Way like spiral, classified in NED as SBbc. The *u*-band image of the galaxy highlights a strong star-forming ring, approximately coincident with the end of the bar; the location of SN 2016P lies directly on a bright knot within this region, giving strong evidence of current star formation which is confirmed by the narrow emission lines evident in the SN spectra. Further evidence for strong star formation in this ring is provided by the fact that it has hosted the two previously mentioned core-collapse SNe; the type II SN 2003bl and the He-poor SN Ic-6 2010do. The apparent magnitude of the host galaxy is $M_{B,0} = -21.05$, and the projected radial distance of the SN from the nucleus is 6.9 kpc. Thus this should be a region of high metallicity, similar to or slightly higher than solar.

A7 Ic-7 SN 2016iae

NGC 1532 is a bright edge-on spiral galaxy, classified in NED as SBb pec. It has a strong bulge component, and the disk is clearly disturbed, probably through interaction with a very nearby, high-surface brightness amorphous companion, NGC 1531, which has a recession velocity only 65 km S^{-1} higher than that of NGC 1532. The location of SN 2016iae is quite central; outside the bright bulge region but on the inner disk, with a projected separation from the nucleus of 3.0 kpc. However, the true separation is uncertain given the edge-on orientation of the galaxy. NGC 1532 is a luminous spiral galaxy, with an absolute magnitude of $M_{B,0} = -21.18$ mag for our adopted distance, and thus the metallicity at the SN location is likely to be high, probably somewhat above solar. Three supernovae have been observed in NGC 1532. The Type II SN 1981A, SN 2016iae, and the Type II SN 2016ija (Tartaglia et al. 2018), which exploded serendipitously during our observing campaign.

A8 Type IIb(I) SN 2017ixz

The host galaxy of SN 2017ixz, 2MASX J07470232 + 2646347, was observed on 2015 November 7th by the Mapping Nearby Galaxies at APO (MaNGA) survey (Bundy et al. 2015), Fig. A1. It was observed with the larger integral field unit (IFU) bundle, which provides with a coverage of 30 × 30 squared arcsec, which practically covers the whole extent of the galaxy. Following (Galbany

et al. 2014) procedures, we analysed both the local environment of the SN within the galaxy and the integrated properties of the host.

SN 2017ixz exploded close to a bright region in the outskirts of its host galaxy. We measure an absolute star formation rate of $3.681 \pm 0.122 \ 10^{-2} \ M_\odot \ yr^{-1}$ at the SN location, an SFR density of $0.016 \pm 0.034 \ M_\odot \ yr^{-1} \ kpc^{-2}$, with a subsolar oxygen abundance of $12 + \log_{10}(O/H) = 8.38 \pm 0.12$ dex (in the Marino et al. 2013 O3N2 scale) and an average stellar age of $\log(A) = 7.01 \pm 1.51$ indicating a high content of young stars at the SN environment. For 2MASX J07470232 + 2646347 we got a total stellar mass of $\log(M_*) = 10.77 \pm 0.07$ dex, and the corresponding values for the oxygen abundance (in the same scale) of 8.51 ± 0.11 dex, an SFR of $2.618 \pm 0.679 \ M_\odot \ yr^{-1}$ and SFR density $0.004 \pm 0.001 \ M_\odot \ yr^{-1}$ kpc^{-2}, and an average stellar age of $\log(A) = 8.32 \pm 1.26$ dex. Our results indicate, that the SN is on a metal-poorer region compared to the average of its host (as expected from its large offset from the core; 6.9 kpc), in an environment with stars that are on average younger than in other locations of the galaxy, and with a higher rate of star formation density. All these parameters are in agreement with the typical environments of SNe IIb (Galbany et al. 2018): outskirts of the galaxy with no high SFR, and young populations with low metallicity.

[1]*Astrophysics Research Centre, School of Mathematics and Physics, Queen's University Belfast, BT7 1NN, UK*

[2]*Astrophysics Research Institute, Liverpool John Moores University, IC2, Liverpool Science Park, 146 Brownlow Hill, Liverpool L3 5RF, UK*

[3]*Department of Physics, Florida State University, Tallahassee, FL 32306, USA*

[4]*Max-Planck-Institut für Astrophysik, Karl-Schwarzschild-Str 1, D-85748 Garching, Germany*

[5]*Department of Physics & Astronomy, University of Sheffield, Sheffield, S3 7RH, UK*

[6]*The Oskar Klein Centre, Department of Astronomy, Stockholm Univsersity, AlbaNova, SE-106 91 Stockholm, Sweden*

[7]*Max-Planck-Institut für Extraterrestrische Physik, Giessenbachstraße, D-85748, Garching, Germany*

[8]*Institute for Astronomy, University of Hawai'i, 2680 Woodlawn Drive, Honolulu, HI 96822, USA*

[9]*Institute of Space Sciences (ICE, CSIC), Campus UAB, Carrer de Can Magrans s/n, E-08193 Barcelona, Spain*

[10]*Institut d'Estudis Espacials de Catalunya (IEEC), C/ Gran Capitá 2-4, Edif. Nexus 201, E-08034 Barcelona, Spain*

[11]*School of Physics, O'Brien Centre for Science North, University College Dublin, Belfield, Dublin 4, Ireland*

[12]*PITT PACC, Department of Physics and Astronomy, University of Pittsburgh, Pittsburgh, PA 15260, USA*

[13]*Department of Particle Physics and Astrophysics, Weizmann Institute of Science, Rehovot 76100, Israel*

[14]*Tuorla Observatory, Department of Physics and Astronomy, University of Turku, FI-20014 Turku, Finland*

[15]*Las Cumbres Observatory, 6740 Cortona Dr. Suite 102, Goleta, CA 93117, USA*

[16]*Department of Physics, University of California, Broida Hall, Santa Barbara, CA 93111, USA*

[17]*Department of Physics and Astronomy, University of Southampton, Southampton, SO17 1BJ, UK*

[18]*Department of Physics and Astronomy, University of Leicester, University Road, Leicester LE1 7RH, UK*

[19]*Istituto Nazionale di Astrofisica – Osservatorio Astronomico di Roma, Via Frascati 33, I-00040, Monteporzio Catone, Italy*

[20]*Kavli Institute for the Physics and Mathematics of the Universe, Todai Institutes for Advanced Study, the University of Tokyo, Kashiwa 277-8583, Japan*

[21]*Millennium Institute of Astrophysics, Nuncio Monseñor Sótero Sanz 100, Providencia, Santiago, Chile*

[22]*Departamento de Astronomía, Universidad de Chile, Camino el Observatorio 1515, Santiago, Chile*

[23]*Departamento de Ciencias Fisicas, Universidad Andres Bello, Avda. Republica 252, Sazié, 2320, Santiago, Chile*

[24]*Harvard-Smithsonian Center for Astrophysics, 60 Garden Street, Cambridge, MA 02138-1516, USA*

[25]*University of North Carolina, 269 Phillips Hall, CB 3255 Chapel Hill, NC 27599, USA*

[26]*Space Telescope Science Institute, 3700 San Martin Drive, Baltimore, MD 21218, USA*

[27]*Department of Physics and Astronomy, Johns Hopkins University, Baltimore, MD 21218, USA*

[28]*Nordic Optical Telescope, Apartado 474, E-38700 Santa Cruz de La Palma, Spain*

[29]*Koninklijke Sterrenwacht van België, Ringlaan 3, 1180 Brussels, Belgium*

[30]*Institute of Astronomy, KU Leuven, Celestijnenlaan 200D, B-3001 Leuven, Belgium*

[31]*LSST, 950 N Cherry Ave, Tucson, AZ 95719, USA*

[32]*Department of Physics, University of California, Davis, CA 95 616, USA*

[33]*GEPI, Observatoire de Paris, PSL Universite, CNRS, 5 Place Jules Janssen, F-92190 Meudon, France*

[34]*Physics Department, Lancaster University, Lancaster LA1 4YB, UK*

This paper has been typeset from a TEX/LATEX file prepared by the author.